LASER INDUCED BREAKDOWN SPECTROSCOPY OF GASES AND AEROSOLS: FUNDAMENTAL STUDIES AND ANALYTICAL APPLICATIONS

By

EMILY MEHGAN GIBB

A DISSERTATION PRESENTED TO THE GRADUATE SCHOOL
OF THE UNIVERSITY OF FLORIDA IN PARTIAL FULFILLMENT
OF THE REQUIREMENTS FOR THE DEGREE OF
DOCTOR OF PHILOSOPHY

UNIVERSITY OF FLORIDA

2004

Dedicated to Granny Payne and Mom and Dad for their love, support, and guidance.

ACKNOWLEDGMENTS

I would like to thank my advisor, Dr. James Winefordner, for being a wonderful mentor and for encouraging me to continue teaching in any way I can. I would like to thank Dr. Nico Omenetto for all his helpful discussions and teachings in spectroscopy but most importantly for his contagious enthusiasm for science. I would also like to acknowledge Dr. Vlasta Horvatic for explaining every derivation so clearly, for helping me see my data from all directions, and most of all for her friendship. I would additionally like to thank Dr. Igor Gornushkin for all his teachings and helpful experimental advice. I would also like to thank Dr. Ben Smith for keeping a smile on my face, giving me hope, and not kicking me out of his office when I am asking him what must seem like the millionth question.

I would also like to thank Dr. David Hahn for sharing his knowledge of LIBS of aerosols and for letting me work with him. I also want to thank Jorge Carranza for teaching me all of the intricacies behind LIBS of aerosols and for being so much fun to work with.

I also want to acknowledge Danielle Dickinson for patiently sharing her knowledge about spores both in helpful discussions/tutorials and by letting me tag along while she grew spores and for providing spore samples.

I would lastly like to acknowledge my family and friends. I want to thank all Winefordner and Harrision group members current and former. I want to thank Tiffany Correll and Jamshid Temirov, for helping me survive this past few years. I would

especially like to thank Tiffany for sharing her knowledge of spectroscopy, which is beyond her years and for her wonderful friendship. I want to thank Jamshid for sharing his amazing knowledge of computers and for also being such a great friend. I would like to thank Danielle for her friendship and for lending her ear whenever I needed it.

I would especially like to thank Leslie O'Neil and Gina Gugluizza for putting up with me and for their wonderful friendship. I also want to thank Laural Reitfert, and Emily Plowman for their amazing friendship and support.

I especially want to thank my parents for not only supporting and loving me at all times but for inspiring me and pushing me to go beyond my expectations. I would also like to thank my brother for his support and love. I want to thank my grandmother not only for loving me but also for teaching me that seeing the good in everyone is the true secret to happiness.

I would lastly like to thank Adam Snyder, who has been a part of my life for a short time but whose love and support have surpassed all my expectations. I also want to thank him for putting the past few months in perspective. I lastly also want to acknowledge him for his editing assistance.

TABLE OF CONTENTS

Page

ACKNOWLEDGMENTS iii

ABSTRACT vii

CHAPTER

1 INTRODUCTION 1

2 FUNDAMENTALS OF LASER INDUCED BREAKDOWN SPECTROSCOPY OF GASES AND AEROSOLS AND RECENT DEVELOPMENTS IN APPLICATIONS AND PLASMA DETERMINATIONS 2

- Historical Background 2
- Fundamentals 2
  - Physics of Laser Induced Breakdown 2
  - Spectroscopic Principles 5
  - Boltzmann Temperature Determinations 5
  - Saha Determinations 6
- Fundamental Studies and Applications 7
  - Recent Fundamental Studies 7
  - Recent Applications 13

3 CURVE OF GROWTH METHODOLOGY APPLIED TO LASER INDUCED BREADKDOWN SPECTROSCOPY PLASMAS OF GASES 30

- Introduction 30
- Background 31
- Theory 33
- Experimental 38
  - Instrument setup 38
  - Gas Introduction and Mixing System 40
  - Analyte and Mixing Gas Selection 41
- Results and Discussion 44
- Conclusions and Future Work: 79

4 LASER INDUCED BREAKDOWN SPECTROSCOPY AS A DETECTOR FOR SPORES.....81

Background.....81
Theoretical Considerations.....84
Experimental.....88
Spore Samples.....88
LIBS Setup.....89
Single Spore Detection.....89
Bulk Analysis.....93
Results and Discussion.....95
Single Spore Detection.....95
Bulk Analysis.....99
Conclusions and Future Work.....105

LIST OF REFERENCES.....110

BIOGRAPHICAL SKETCH.....117

Abstract of Dissertation Presented to the Graduate School
of the University of Florida in Partial Fulfillment of the
Requirements for the Degree of Doctor of Philosophy

LASER INDUCED BREAKDOWN SPECTROSCOPY OF GASES AND AEROSOLS: FUNDAMENTAL STUDIES AND ANALYTICAL APPLICATIONS

By

Emily Mehgan Gibb

May 2004

Chair: James Winefordner
Major Department: Chemistry

Considerable research has been done on the analysis of single particles in Laser Induced Breakdown Spectroscopy (LIBS); however, plasmas formed in gases or aerosols at atmospheric pressure have not been sufficiently characterized. It has previously been determined that the introduction of particles into a gas plasma does not significantly change parameters such as plasma excitation temperature. This infers that once fundamental parameters of an air plasma are determined, then these same parameters would apply to a plasma encompassing a single particle. Curve of growth (COG) methodology provides information regarding spectral broadening processes for absorption and emission measurements in flames and has recently been implemented for the resonance transition of chromium in LIBS analysis of stainless steel standards. In this work the curve of growth methodology was applied to a plasma formed in a gaseous sample, a mix of carbon dioxide, CO_2, and argon, and the curves were generated using the non-resonance transitions of C(I), at 193.0905 nm and 247.8561. These transitions were selected because they undergo self absorption and emit radiation in the ultraviolet and visible region, the region of detection for typical LIBS instrumentation. The applicability of this theory to LIBS of gas plasmas was assessed. The experimental calibration plots plateaued and decreased, not allowing the broadening effects to be elicited through the curve of growth method. Diagnosis of the cause behind the unusual calibration plots was performed using additional experiments examining the oxygen emission, and examining the line broadening of both of these transitions. The dissociation fraction of the CO_2 changed as more CO_2 was added. Broadening processes in the plasma were able to be determined and the instrumental requirements to utilize COG theory were ascertained.

The threat of additional terrorist attacks with biological agents such as anthrax has placed detection of bioaerosols and specifically bacillus spores at the forefront of LIBS applications. The possibility of using LIBS for detection of single spores was explored theoretically and the analysis of single spores of *Bacillus licheniformis* was performed with an intensified charge couple device (iCCD). Limitations of the method for single spore analysis were also determined.

CHAPTER 1
INTRODUCTION

This work focused on further characterizing the aerosol plasma and developing LIBS as a detector for *Bacilllus* spores.

In Chapter 2, background on Laser Induced Breakdown Spectroscopy (LIBS) is given focusing on LIBS of gases and aerosols. First the fundamentals of breakdown in gases and aerosols are discussed and then the spectroscopic principles of LIBS plasmas are also reviewed. Recent work done on plasma parameters and developments in LIBS based applications for gas and aerosol analysis are also presented.

Chapter 3 gives background on the curve of growth (COG) method and broadening processes. The reasons behind the choice of the analyte gas, carbon dioxide, and the mixing gas argon are presented. The experimental assessment of the applicability of the theory to LIBS plasmas of gases is presented. Broadening parameters are shown and explanations of the experimental data are given. Instrumental modifications are suggested for assessing the true potential of the curve of growth theory for determination of plasma parameters.

The current techniques for *B.* spore detection are shown and their advantages and limitations are discussed in Chapter 4. Principles behind the detection of spores with LIBS are discussed. Additionally, single spore detection of *B. licheniformis* is accessed and the particle size distribution of the aerosol generated from the spore solutions is presented. Spectra from spores taken on a substrate are presented and are analyzed via principal component analysis. The potential and limitations of the technique are also discussed.

CHAPTER 2
FUNDAMENTALS OF LASER INDUCED BREAKDOWN SPECTROSCOPY OF GASES AND AEROSOLS AND RECENT DEVELOPMENTS IN APPLICATIONS AND PLASMA DETERMINATIONS

Historical Background

The development of the ruby laser by Theodore Maiman in 1960 [1] led to the first laser induced plasma (LIP) in 1962.[2] In subsequent years, Maker and coworkers formed a laser induced plasma in air.[3] The technique was explored mainly by physicists and there was limited exploration into its analytical capabilities until the 1980s. There are many excellent reviews on laser induced plasma spectroscopy (LIPS), or, as it is otherwise known, laser induced breakdown spectroscopy (LIBS), for work done prior to 1997.[4;5] Also a textbook has been written on the subject[6] and two comprehensive reviews have been published that focus on LIBS of aerosols and gases.[7;8] The focus of this work is to review the fundamentals of LIBS of gases and aerosols and present some recent research into the fundamentals and applications of LIBS of gases and aerosols.

Fundamentals

Physics of Laser Induced Breakdown

In LIBS, a laser is focused through a lens to form a plasma either on a target or in air. Seed electrons, created by multiphoton ionization or electron tunneling, in the plasma will undergo cascade growth when they absorb laser radiation via inverse Bremsstrahlung collisions. These electron-neutral species collisions, between electrons and surrounding gas molecules, facilitate the absorption of photons of laser energy. This cascade growth, also termed avalanche ionization, causes the electron density to increase exponentially in the region in which the laser is focused and a plasma to be generated. This plasma then expands towards the focusing lens, forming a spherical shock wave.

The generation of seed electrons is highly sample dependent. For gases, the wavelength and irradiance of the laser determine the type of mechanism that generates the initial electrons. At longer laser wavelengths, $\lambda > 10$ μm and high irradiances, the primary mechanism of electron generation is electron tunneling. This occurs because the electric field generated by the laser radiation is strong enough to pull an electron out of the atoms outer shell.[6]

Cosmic rays or radioactivity may produce electrons in ambient gas. The concentration of electrons in ambient air is 10^3 cm^{-3} but only 10 electrons are produced per second, meaning, in the nanosecond (or less) pulse regime typically used in LIBS, this is too slow to be the primary mechanism of initial electron generation.[9]

At shorter wavelengths, typically less than 1-2 μm depending on laser irradiance, multiphoton ionization provides the initial electron. This mechanism involves simultaneous absorption of a number of these shorter wavelength photons from the laser radiation causing ionization of the gas molecules and which creates electrons. Eight and ten photons of 1064 nm radiation, the typical wavelength of laser radiation used in LIBS measurements, are necessary for multiphoton ionization of major ambient air components O_2 and N_2, respectively. A simple expression was derived by Grey Morgan[10] for the breakdown threshold flux intensity, that is, the flux necessary to cause a visible breakdown assuming only the multiphoton ionization process. This flux intensity, F_{th}, in photons s^{-1} cm^{-2}:

$$F_{th} = \frac{\nu}{\sigma}\left(\frac{\delta k!}{\tau \nu}\right)^{\frac{1}{k}} \qquad [1]$$

where ν is the frequency of the laser in s^{-1}, σ is the absorption cross section of a single photon of the laser radiation in cm^2, δ is the fraction of ionized atoms necessary for breakdown, k is the number of photons that are needed for multiphoton ionization, τ is the laser pulse duration in s. The assumptions used to generate this simplified expression include the lifetime of each virtual state is $1/\nu$, the value for $F_{th}\sigma/\nu$ is much less than one, and the photons of laser radiation follow a Poisson spatial distribution. Due to the wavelength and irradiance ranges used for most applications in LIBS of gases and aerosols, multiphoton ionization is the predominant mechanism for initial electron generation.

It is known that presence of particles in the focusing volume will decrease the breakdown threshold, which, is the irradiance required for breakdown to occur in more than 50 percent of the laser focusing events, by approximately 100 times thresholds found for plasmas formed in pure gases.[11] The breakdown process becomes even more complex because particles provide sites for photons of laser radiation to be absorbed.[12] If the particles are transparent then the particles may further focus the laser beam, a process that is termed self-focusing. All particles will still reduce the breakdown threshold by causing thermoelectric emission, local heating on the particles surface,[13] and, if the particle size is such that the incoming laser beam is in resonance with the Mie scatter of the particles, further enhancement of the breakdown process occurs.[14] When the plasma does form with a particle or particles in the focal volume, the particles are vaporized, and the contents are excited and ionized and the plasma propagates towards the focusing lens forming an elliptically shaped plasma.[15]

Spectroscopic Principles

Plasma emission is isotropic and early times in the plasma evolution are dominated by continuum radiation resulting from the inverse Bremsstrahlung emission produced by collisions between the neutrals and the electrons. Emission from ionic species is prevalent at early times in the plasma evolution while emission from the atomic species is still observed at much later times in the plasma. The emission from the plasma may be collected via a fiberoptic or a lens which delivers the plasma radiation to a spectrometer. The dispersed light may be detected by a variety of detectors including intensified and non-intensified charge coupled devices (iCCD and CCD), photomultipliers (PMT), and photodiode arrays. Gated detectors are preferred due to large continuum that contributes to an increased background signal at early times in plasma evolution.

The LIBS plasma has a high electron density, $n_e > 10^{16}$ cm^{-3}, allowing for collisional processes to dominate relative to radiative processes and hence allowing local thermodynamic equilibrium to exist in the plasma.[16] This allows for relationships such as the Boltzmann and Saha equations to be used to calculate plasma parameters such as excitation temperature and populations of excited states.

Boltzmann Temperature Determinations

In LIBS, plasma temperature determinations are important to understanding the evolution of the plasma. If local thermodynamic equilibrium is assumed to exist for the levels of interest, the simplest way of determining plasma temperature relies on the principle that atoms are distributed in the respective states according to Boltzmann relationship.[17]

$$\frac{n_j}{n_i} = \frac{g_j}{g_i} e^{\frac{-(E_j - E_i)}{kT}} \qquad [2]$$

The number density of atoms in the lower and upper states are give by n_i and n_j in cm^{-3}, the degeneracies of the lower and upper states are give by g_i and g_j, the energy levels of lower and upper states are given by E_i and E_j in J, k is Boltzmann's constant in K^{-1} J, and T is the plasma temperature in K. The Boltzmann relationship can be rewritten in terms of relative intensity ratios by the following:[17]

$$\frac{I_\lambda(1)}{I_\lambda(2)} = \frac{A_{ji}(1)\, g_j(1)\, \lambda_0(2)}{A_{ji}(2)\, g_j(2)\, \lambda_0(1)} e^{-\left[\frac{E_j(1) - E_j(2)}{kT}\right]} \qquad [3]$$

where I_λ is the spectral intensity of the each line, A_{ji} is the transition probability of the transition in s^{-1}, g_j is the degeneracy of the transition, E_j is the upper energy level of the transition in J and λ_0 is the wavelength for the transition of interest in cm. Measurements of spectral intensity are taken for a variety of spectral transitions to construct a plot of $ln(I_\lambda \lambda_0 / g_j A_{ji})$ versus upper energy level of the transition. When linear regression is performed on these lines a slope of $-1/kT$ is generated. Problems inherent to this method include inaccuracies in tabulated transition probabilities, inability to find spectral lines with significantly different upper energy levels in a single spectral window, and errors in intensity measurements resulting in larger errors in temperature measurements.[18]

Saha Determinations

If local thermodynamic equilibrium is established in the plasma, the number density of atoms, n_a in cm^{-3} , and ions, n_{a+1} in cm^{-3}, in the plasma volume and the number density of electrons, n_e in cm^{-3}, in the plasma volume are all governed by the Saha expression. [18]

$$\frac{n_e\, n_{a+1}}{n_a} = \frac{2(2\pi mkT)^{\frac{3}{2}}}{h^3}\,\frac{Z_{a+1}(T)}{Z_a(T)}\,e^{-\frac{Eion}{kT}} \qquad [4]$$

In this equation m is the mass of the electron in kg, k in Boltzmann's constant in J K^{-1}, h is Planck's constant in J s, $Z_{a+1}(T)$ and $Z_a(T)$ are the partition functions for the ion and atom states, E_{ion} is the ionization energy in J and T is the plasma temperature in K. This equation may be used to find the total populations in the atomic and ionic states.

Fundamental Studies and Applications

Recent Fundamental Studies

In the 1990s, the primary focus of fundamental studies was on determining breakdown thresholds, plasma excitation temperatures, and the number density of electrons in the plasma for a variety of gases. Further insight into the dependence of these factors on laser wavelength and experimental parameters was also explored. The dependence of the breakdown threshold on laser spot size, gas pressure, and pulse duration was ascertained for various wavelengths of laser radiation. [19] The effect of increasing the pressure of the ambient gas inside the LIBS chamber was a decreased the breakdown threshold, with the plot of peak threshold intensity, in W/cm^2, versus gas pressure, in torr, generating slopes of -0.4 to -0.8 for the laser radiation ranging from 1064-355 nm, which is in close agreement with previous studies. This indicated that multiphoton ionization was the mechanism for plasma formation at shorter wavelengths whereas for the longer wavelength of 1064 nm the formation proceeded due to cascade and collisional ionization. This work further confirmed that there was a weaker dependence on pulse length for the 1064 nm radiation from a pulsed Nd:YAG than for the frequency doubled 532 nm, tripled 355 nm, and quadrupled 266 nm radiation. Threshold intensities also were smaller for larger laser focal spot sizes.

Breakdown thresholds and their dependence on gas pressure were determined for LIBS plasmas in xenon, argon, nitrogen, and oxygen.[20] In these experiments, the breakdown threshold was defined as the irradiance at which 25% of the laser shots produced a visible plasma. These values were compared to three other previous studies done with an identical laser and a focusing lens with a similar focal length and spherical aberration. There was a factor of 4 difference between the measurements due to different criteria for breakdown and differing beam waist sizes. When ratios of the thresholds between the different gases were examined, only a 2 fold difference between the experiments was observed. The breakdown thresholds were the lowest for xenon and were the highest for argon and oxygen. The wavelength of laser radiation had the most significant effect at the higher gas pressures and the threshold dependence on pressure was most significant for the 1064 nm radiation. This supported the theory that cascade ionization via electron collisions, and not multiphoton ionization, played the largest role in electron generation during plasma formation.

The evolution of a plasma, generated with a Nd:YAG pulsed laser whose pulse output was modified by a regenerative amplifier frequency doubling crystal to form a 60 ps pulse width at 532 nm, was examined by probing it in a collinear geometry with a dye laser.[21] This allowed absorption by the plasma to be examined as a function of plasma evolution. Plasmas formed in helium, argon, and nitrogen were investigated. Breakdown was observed in the middle of the temporal arrival of the laser pulse and growth of the plasma continued after the termination of the laser pulse in low pressure atmospheres of nitrogen and argon. However, in high pressure atmospheres of all the gases, breakdown was observed even earlier than with the lower pressures and the plasma was more intense.

Breakdown thresholds, excitation and ionization temperatures, and electron number densities were determined for plasmas created in carbon monoxide and carbon dioxide.[22] Various wavelengths of laser radiation were investigated including 266 nm, 355 nm, 532 nm, and 1064 nm from harmonics of the pulsed Nd:YAG and the 193 nm from an ArF - excimer laser. Thresholds were found to be approximately the same for all wavelengths in air, carbon monoxide, and carbon dioxide; however, for plasmas formed using the 193 nm laser radiation, the breakdown threshold was greatly reduced. The laser radiation at 193 nm was able ionize carbon through a 2 photon process. An example of this is that the breakdown thresholds ranged from $1.0\text{-}3.0\times10^{10}$ for carbon dioxide plasmas formed using the harmonics of the Nd:YAG but were 1.2×10^{9} for the 193 nm radiation.

Another significant discovery was that the electron number density was not dependent on the laser wavelength or the gas composition. The excitation temperatures were, however, slightly different. This was attributed to the larger plasmas formed with the 1064 nm radiation and to the cooler regions that are also averaged into the overall plasma temperature. The plasmas created with shorter wavelengths are smaller and do not have these cooler areas. Ionization temperatures determined from the electron densities were also in close agreement regardless of the wavelength of laser radiation or the gas composition.

Mathematical modeling of a LIBS plasma formed in a nitrogen and oxygen gas mixture was used to further elicit processes in plasma evolution.[23] This model was based on “inverse Bremsstrahlung radiation theory” and was able to generate information regarding populations of excited states, maximum electron densities, and breakdown thresholds for plasmas generated from 4 laser wavelengths: 308 nm, 694 nm, 1064 nm, and 10.6 μm. The simulation model gave three significant trends in plasma formation: plasmas induced by UV lasers developed via multiphoton ionization while plasmas induced by IR lasers developed via cascade ionization from electron collisions, lower breakdown thresholds were observed for shorter wavelengths of laser radiation due to more efficient multiphoton ionization, and finally, at the breakdown threshold, the energy deposited into the plasma was transferred to the vibrational and excited states of molecules.

In a separate study, Mie theory was used to model experimental angular distributions of scattered radiation during the laser induced breakdown in air.[24] Scattered radiation was observed for LIBS plasmas created using the Nd:YAG harmonics of 1064 nm, 532 nm, and 355 nm. The entire plasma as a whole could not be modeled due to its inhomogeneity but the plasma could be modeled as a collection of sub micrometer plasma balls.

An additional model to investigate the breakdown process was based on the numerical solution of the time dependent Boltzmann equation for plasmas generated in nitrogen.[25] The generated breakdown thresholds agreed well with previous experimental findings. They also further confirmed that for plasmas created with 355 nm laser radiation, the losses due to the deposition of energy into the vibrational states of molecules were dominant at the time of breakdown. This model also found that collisional ionization played a minor role in the breakdown process in comparison to multiphoton ionization for the laser wavelengths of 532 nm and less. Again for laser radiation at 1064 nm, plasma breakdown occured due to collisional ionization and multiphoton ionization.

Perhaps the most significant fundamental studies of the laser spark in air were carried out by Yalcin and coworkers.[26] In these studies, the effects of ambient conditions on the plasma were investigated. Temperature determinations were performed using a graphical plot, which was generated through a combination of the spectral intensities in the Saha and Boltzmann relationships. They were able to obtain more accurate temperature measurements by obtaining more data points and a larger spread in the energy levels of the transitions. They also compared temperatures and electron number densities obtained using path integrated emission measurements, which gave the average emission seen from all regions of the plasma, versus the Abel inverted emission measurements, which gave spatially resolved spectra. Electron densities were determined using Stark broadened lines of hydrogen and nitrogen. The Abel inverted measurements yielded slightly higher temperature and electron density values than the path integrated measurements due to the presence of cooler regions of the plasma. Abel inverted measurements were then used for the remainder of the plasma temperature assessments because the path integrated measurements caused greater than 20 percent error.

In this same work, it was determined that the presence of water, metal $MgCl_2$ aerosols, and even the presence of a different gas of SF_6 or He did not significantly affect the plasma temperature at early delay times of 0.35 and 1.4 μs. The effects of laser pulse energies ranging from 40-150 mJ/pulse were also examined. Increasing laser pulse energy by a factor of 3.8 doubled the electron number density but the plasma temperature did not change significantly at these early delay times.

Plasmas in various gases formed from a pulsed ruby laser, with a laser wavelength of 694.3 nm, a laser pulse energy of 1 J, and a 30 ns pulse width, were studied to compare the electron number density and electron temperature of plasmas formed in various gases.[27] Helium, argon, and nitrogen all yielded similar temperatures ranging from, 8330 K for argon to 9800 K for helium. The number densities were determined to be 8.1×10^{16}, 9.46×10^{16}, 3.2×10^{17} cm^{-3} for helium, argon, and nitrogen, respectively, all indicating the presence of local thermodynamic equilibrium.

Spectroscopic features of plasmas formed in air from femtosecond laser pulses, generated by a pulsed Nd YLF laser, at the wavelength of 1053 nm, with a pulse energy of 200 mJ/pulse, and with a 500 fs pulse width, were also recently investigated.[28] In this plasma, predominately molecular lines from N_2 and N_2^+ were observed at early times in the plasma, less than 1 ns, predominately continuum emission was observed at intermediate times, between 1 ns and 100 ns,, and N and O atomic emission lines were observed at times of 5 ns and later.

A recent major development in fundamentals of aerosols was the determination of the upper size limit of particles that can be quantitatively analyzed via LIBS. Radziemski and coworkers determined in the 1980s, using measurements of beryllium particles on filters, that the upper size limit for accurate calibration resided somewhere around 10-15 μm.[15] Carranza and coworkers determined for their laser conditions, a Q-switched pulsed Nd:YAG running at a pulse energy of 320 mJ/pulse with a 10 ns pulse width and a 5 Hz repetition rate, the upper size limit for quantitative analysis and hence complete vaporization , was 2.1 μm.[29] Dilute aerosols of monodisperse silica particles, which were able to give one particle per plasma volume, were used to determine the upper size limit and concentrated solution of silicon (ICP-standards) were also analyzed to insure that self absorption was not the affecting the linearity of the emission signal.

Three reasons were given for the much lower size limit for vaporization of single particles in air. The first was that temperature gradients in the plasma could cause the particle to be moved from hotter regions of the plasma to cooler regions causing incomplete vaporization. Secondly, inhomogeneity in the distribution of the radiation flux on the particle surface could also bring about different rates of vaporization because the differing amounts of surface evaporation were occurring along with phase explosion. These effects would most likely transfer momentum to the particle, again moving it away from the hotter region of the plasma. The last explanation given was that the expansion that typically occurred when the particle was heated did not take place as readily in larger particles, meaning the particle would not break apart into smaller pieces which were in turn easier for the plasma to vaporize.

Recent Applications

LIBS is an attractive analytical method for numerous reasons including minimal sample preparation is needed, remote sensing is possible, instrumentation can be inexpensive and portable systems are now available. Applications of LIBS to gas analysis, however, are greatly outnumbered by applications of LIBS to other types is samples. The main focus in analytical applications in recent years has been halogen detection of fire retardants and refrigerants.[31-33]

Halocarbons, C_2F_5H, CF_4, CF_3H, and CF_2H_2, were detected using a system with a Q switched pulsed Nd:YAG operating at the fundamental wavelength of 1064 nm and at 10 Hz repetition rate using a photodiode array (PDA).[31] These compounds are primarily used in fire extinguishing equipment and their concentrations need to be monitored during fire suppression testing and additionally during tests to establish their effects on the environment. Optimization of argon sheath flow in the sampling tube, laser pulse energy, and positioning of fiber optic was done prior to analysis. Sheath flow of 0.5 scm/min, pulse energy of 120 mJ/pulse and fiber optic positioning of 4.2 mm over the bottom edge of the plasma were the conditions determined as optimal. As determined in earlier work by Cremers in the 1980s, the number of fluorines in a compound is directly proportional to the emission signal.[30] This allowed for the differentiation of the various halocarbon compounds. A detection limit of 40 ppm was determined for CF_4 using the 685.6 nm transition satisfying the requirements for detection of fire retardants, which contain 1-30% halocarbons. In order to monitor multiple compounds, a CCD was suggested as detector in future studies.

This same research group further expanded upon the above analysis by quantitation of: a different fire suppressant, C_3F_7H, a refrigerant, $C_2F_4H_2$ and a compound which was previously analyzed, CF_4.[32] A gated detection system with an intensified photodiode array coupled to a spectrograph was examined for this application. The addition of a gated detector required that the delay time and gate width be optimized and a delay time of 0.6 μs and a gate width of 0.5 μs were optimal. The detection limits were 490, 750, 530 ppm for C_3F_7H $C_2F_4H_2$ and CF_4 respectively.

An iCCD was utilized for the quantitation of low concentrations of fluorine, chlorine, sulfur, and carbon containing gases in air. Detection of chemical warfare agents was the underlying application of this analysis.[33] The analysis was performed using a pulsed Q-switched Nd:YAG operating at the fundamental wavelength, at pulse energies varying from 25-160 mJ/pulse, and at a 50 Hz repetition rate with a 10 ns pulse width.

Delay time, gate width, and the number of accumulated spectra were all optimized. The emission lines used for determination of the limit of detection for sulfur, chlorine, carbon, and fluorine were 921.29 nm, 837.594 nm, 833.515 nm, and 685.604 nm, respectively. Sensitivity was compromised to obtain lines within the same spectral window so that ratios of the elements in these gases could be found, thus also allowing identification of the compounds.

For a 20 s analysis time in which the spectra are allowed to accumulate, detection limits of 20, 90, 26, and 1500 ppm w/w% were found for fluorine, chlorine, carbon, and sulfur respectively. Calibration curves for carbon at different concentrations of various hydrocarbons and fluorine at different concentrations in various halogens were constructed. Using the ratios of the slopes from these calibration curves, the stoichiometric ratio of the carbon and fluorine in the various compounds could be found. Another important finding in these studies was that even stable gases such as SF_6 and CF_4 are completely vaporized by the plasma at the delay times used for analysis, which were around 2 μs.

Research was continued by this same group on analysis of these same compound types. Various factors that affected the sensitivity of this analysis included the number of spectra taken, plasma reproducibility as a function of laser pulse energy, reproducibility of the spatial distribution of atomic emission, and the effect of laser wavelength and energy on plasma emission.[34] One hundred shots of the 1064 nm laser radiation with a pulse energy of 100 mJ/pulse yielded the most sensitive results.

Gas phase metal hydrides, specifically those containing Sn and As, were also analyzed via LIBS.[35] The effects of He and N_2 buffer gases on analysis were investigated. Helium proved to be a better buffer gas giving more than a 6 times enhancement of the signal to background ratio of the Sn emission line for measurements taken in He versus the measurements taken in N_2.

Far more research has been done in the field of aerosol analysis, starting first with filter analysis. Arnold and Cremers detected thalium, a highly toxic metal, on filters using a pulsed Nd:YAG, running at 257 mJ/pulse, with a 10 ns pulse width and a linear intensified photodiode array for detection.[36] Ablation of the filter was desirable to probe particles embedded in the filter and the mass removed by the spark was 25-30 %. Three passes through the filter ablated away all filter material and hence the thalium. The detection limits on the filter were 0.2 μg/filter for the 535.05 nm transition and 1μg/filter for the 377.57 nm transition. It was determined that if air sampling was performed at a rate of 4 L/min, it would take 25 minutes of sampling for LIBS to detect thalium at concentrations one order of magnitude above the detection limit; this corresponded to a mass concentration in air of 0.01 mg/m^3.

The first attempt to overcome the sampling problems associated with analysis of particles by LIBS was done by Schechter.[37] The problems that he felt made aerosol analysis difficult included the different number of particles sampled by each plasma, the different size and composition of the sampled particles, and finally, the location of each particle in the plasma. Instead of delaying his intensified optimal multi-channel analyzer to decrease the background of the air continuum, he attempted to fit the baseline to a function. He used this function in his algorithm to obtain the spectrum with the most intense lines from the analyte particle. His algorithm was composed of three parts: first, reject all spectra that did not possess analyte emission lines; second, reject all spectra where the fitted baseline was too weak or too intense to be compared to the average spectra of clean air; and lastly all spectra but the 25 percent that had the most intense analyte emission lines are thrown out. For a zinc aerosol the limit of detection for zinc using the 481.05 nm transition was 1.3 percent when the algorithm was implemented versus 4.1 percent if all spectra were used. A discussion of how the algorithm affected sampling statistics was not given.

The first field test using LIBS involved toxic metals in stack effluents.[38] This particular LIBS setup possessed a frequency-doubled Nd:YAG operating at 500 mJ/pulse with a pulse rate of up to 5 Hz and a gated photodiode array. Using laboratory generated aerosols, they were able to determine that the minimum concentration of toxic metals that they could detect ranged from less then 0.1 μg/scm for beryllium to 250 μg/scm for lead. The authors proposed that an increased laser power may increase the signal and that the efficiency of light collection for their system could also be improved. The goal of the field tests was three-fold: they wanted to insure that the LIBS system was reliable when operating in the field, that it could measure ppb levels of these metals in the effluent, and that it could provide real time information about toxic metal concentration. Calcium, boron, silicon, cadmium and manganese were all detected in the waste feed from a glass melt. Higher stir speeds of the glass melt seemed to decrease the amount of metals detected, which reflected LIBS capabilities to do real time monitoring.

More field tests were performed with two LIBS systems to monitor effluents in different regions in the stack. [39] The first detector was an intensified diode array detector (iPDA) with the second detector being an intensified charge coupled device (iCCD). A frequency doubled Q-switched Nd:YAG was utilized in both systems. The systems were calibrated and limits of detection ranged from 1 μg/acm for beryllium to 680 μg/actual cm^3 for mercury with the relative percent standard deviation ranging from 3 % for analysis of beryllium to 15 % for analysis of zinc. Field tests were performed at a facility where the simulated wastes were generated and the LIBS system was placed before the HEPA filter and the stack. Typical sampling times were 50 s for these tests, corresponding to 500 laser pulses. Concentrations much over the limit of detection ranging from 525-122704 μg/scm, for Ce, N, Pb, Se, Hg, and Cr were set to be the alarm levels and the LIBS system was tested. The LIBS system was able to detect when the toxic metals reached alarming levels in the effluent. Concentrations of Pb, Fe, and Cr were also determined for a waste stimulant placed in a torch hearth.

The results were compared to traditional chemical methods and reasonable agreement was seen between the two techniques except for the LIBS signal for chromium was artificially high due to the CN band spectral interference at the chosen chromium transition. LIBS measurements were also made to test the efficiency of a ceramic filter in a Slip Stream Test Bed. One LIBS system was placed before the ceramic filter and one was placed after the filter to estimate the partitioning of the Mn, Cd, Zn, and Sn through the filter and to determine the metal removal efficiency of the filter.

A conditional analysis algorithm for aerosols was developed by Hahn and coworkers.[40] The initial work done focused on defining the particle sampling rate of LIBS and constructing the conditional analysis algorithm. The particle sampling rate, *PSR*, was defined as:

$$PSR = (1 - e^{-\mu}) \times 100 \qquad [5]$$

where μ is the average number of particles per spark. This average number may be determined from the overall mass concentration of the metal, x in g/m^3, the density of the metal particle, ρ in g/cm^3, the volume of the plasma, V_{Plasma} in cm^3, and the mean diameter of the particle, d_{VMD} in m. This relationship is shown in the following equation:

$$\mu = \frac{6\, x\, V_{Plasma}}{\pi\, \rho\, d_{VMD}^3} \qquad [6]$$

Using these equations and typical values for the concentrations of metals in aerosols from stack effluents and ambient aerosols and the sizes of these aerosol particles, he was able to show that particle sampling rates were very low.

The implementation of a conditional analysis algorithm takes advantage of the large signals sometimes seen for single spectra of an aerosol particle. Conditional analysis rejects spectra not containing emission lines for the particle of interest leaving only spectra that contain signal from the analyte particles. Monte Carlo simulations were performed to address the two main issues in particle sampling. The first was how many sampled particles are needed to obtain accurate size distributions and secondly how many sampled particles are needed to give an accurate value of the number density of the particles in the air. Only 20 particles had to be sampled to obtain accurate measurements, meaning, the actual concentration of the metal in the air, C in µg/m^3, can be determined from the product of the average metal concentration for the hits, x in µg/m^3, which was determined from the ensemble average of the hits, and the sampling frequency of the hits, F. For the particle sampling statistics to be viable, the number of laser shots taken for the measurements should be determined by the number of laser shots and not by the number of hits.

This algorithm was implemented for detection of iron, chromium, and manganese, utilizing a LIBS system with a Q-switched Nd:YAG operating at the fundamental wavelength, at a repetition rate of 5 Hz and at a pulse energy of 300 mJ/pulse, with a 10 ns pulse width. A series of 1000 laser shots was taken and the observed plasma emission was collected in backscatter geometry and detected by a spectrograph coupled to a gated iCCD. The emission signal was normalized to the continuum in both the calibration and the sample measurements. This normalization termed peak to base, improved the precision in the LIBS measurements. Single shot spectra were obtained and the average of these single spectra, termed the ensemble average, was also obtained. The manganese concentrations, determined through LIBS analysis, were equivalent to the concentration determined using an EPA standard method.

This same system was again used to further expand the applicability of the conditional analysis algorithm.[41] The volume of the plasma, under the same conditions as the previous work except at a higher laser power of 400 mJ/pulse, was ascertained using a dilute aerosol of monodisperse polystyrene/divinylbenzene particles which contained a known percentage of Fe_3O_4. Since the concentration of the aerosol was adjusted to a single particle being sampled per plasma, the particle diameter and density were known, and the mass concentration was known, the volume of the plasma could be determined.

This plasma volume, 2.5×10^{-4} cm^3, was then used to determine the size distribution of the same monodisperse aerosol using the iron emission signal. As seen above in equation 6, if a calibration curve was generated for the emission signal for iron versus the mass concentration, the size distribution could be determined. The mean diameter of the size distribution was 0.932 μm with a standard deviation of 0.090 μm which was very close to the actual particle size of 0.940 μm. This same method was used to generate size distributions for particles containing magnesium found in ambient air. The particles chosen were assumed to be $MgCO_3$ so that the size distribution could be determined from the magnesium emission lines. The problems associated with detection of different types of particles containing the same element based on the analysis of size distributions were also discussed.

More particle size distributions for both monodisperse aerosols of calcium and magnesium were also constructed using this same system.[42] These size distributions were in good agreement with laser aerosol spectrometer (LAS) measurements. This algorithm was based on prior knowledge of the particle's constituents. Without information regarding the elemental composition of the particle, which was likely due to the small wavelength range of the spectral windows used in these experiments, the composition had to be guessed. The authors discussed in this work that minimum error in the size distribution is incurred due to the cube root dependence of the particle diameter on the particle density.

The concept of using two emission lines in the conditional analysis instead of setting an acceptable value for false positives was also discussed. Using this approach, the smallest detectable calcium or magnesium particle was 175 nm corresponding to a mass of 3 fg for these analytes. The effects of the presence of multiple particle types were also examined. Size distributions of chromium and calcium particles in a polydisperse solution were constructed using emission lines within the same window.

The particle size distributions agreed with the other methods such as LAS and particle collection with subsequent analysis by scanning electron microscopy.

A large percentage of aerosol particles are not metallic. An example of these are sulfuric acid aerosols. The detection of sulfuric acid aerosols was attempted using a LIBS system with a pulsed Nd:YAG operating at the fundamental wavelength, at a 10 Hz repetition rate and at a pulse energy of 78 mJ/pulse, with a pulse width of 6 ns.[43] Using a delay time of 6 μs and a gate width of 3 μs on the optical multichannel analyzer detector, a sulfur detection limit of 0.38 ppm by volume was achieved for the 182.034 nm transition with an accumulation of 600 shots. This transition is far enough in the vacuum ultraviolet (VUV) region that the atmospheric oxygen is absorbing the plasma emission at this wavelength. This problem was averted by flowing 20 L/min of nitrogen through the spectrometer. Subsequently, the addition of a buffer gas of argon for analysis along with the spectrometer purge yielded a lower detection limit of 27.4 ppbv in the same analysis time. The photofragmentation experiments performed along with the LIBS measurements yielded a detection limit of 46.5 ppbv in a shorter analysis time of 10 s.

In the aluminum processing industry, the monitoring of gaseous and particulate fluorides is important not only for improving the smelting process but also for protecting the health of those working in and around these plants. Tran and coworkers[44] analyzed fluorine in gas with SF_6 as the sample, aerosol fluoride particles with NaF as the sample, and fluoride particles on filters with NaF as the sample. The LIBS system used in this analysis consisted of a pulsed Q-switched Nd:YAG operating at the fundamental wavelength of 1064 nm , at a 1 Hz repetition rate and with a 5 ns pulse width, and a spectrometer coupled to an iCCD. Improvement of the limits of detection of fluorine was achieved by using helium as a buffer gas. Different configurations for introduction of helium gas were tested including: mixing the sample containing fluoride and air with helium, using a helium sheath flow, and having only helium and the fluoride aerosol sample present. The lowest detection limits, of 0.1-0.3 mg/m^3, for gas and aerosol fluoride particles were found with pure helium. Filter analysis with air and helium as the surrounding gas at atmospheric pressure yielded even lower limits of detection, 75.0 to 5.0 μg/m^3, respectively.

More work continues to be done on the detection of metal aerosol in effluents. Now the focus is moving toward system optimization such as studies on the effects of laser wavelength, excitation energy, and delay time.[45] The various harmonics of the fundamental wavelength of Nd:YAG were studied during analysis of chromium with an iCCD. The pulse energies at the various wavelengths were 80, 250, and 500 mJ/pulse for the 266 nm, 532 nm, and 1064 nm radiation, respectively. Optimum conditions for the analysis of chromium were observed when using the frequency doubled Nd:YAG, at a pulse energy of 75 mJ/pulse, and when the iCCD was set to a delay time of 17 μs. These conditions achieved a detection limit of 400 ng/scm for chromium.

In stack emissions monitoring, the rather high limit of detection for mercury by LIBS measurements is a problem because it presently renders the technique not suitable for testing the levels of compliance in new incinerators. It was noticed that presence of oxygen decreases the intensity of the mercury emission line in microwave induced plasmas, leading Gleason and Hahn to investigate this effect in a LIBS plasma.[46] The setup was identical to what was used in previous aerosol determinations.[42] At early delay times (5-10 μs), this decreased signal was not observed when oxygen was added, however, at later delay times (30-100μs), the effect was seen. Temperatures determinations of nitrogen and air, performed via chromium particles introduced into the plasma, indicated that at later delay times, the plasma has cooled to below 10,000 K meaning the oxygen was possibly recombining in the air plasmas. An identical decrease in the mercury emission intensity was observed when CO_2, CO, or air versus nitrogen were present. This indicated that oxygen recombined regardless of the source. Other transitions, 365.02 and 435.83 nm, also did not show a marked decrease in intensity for later times in the plasma. The authors concluded that transition specific quenching by O_2 and NO was occurring in the air plasma causing the mercury emission signal to decrease.

Detection of toxic metals aerosols was further improved by optimization of delay time and gate width for LIBS analysis with a gated iCCD arsenic, beryllium, cadmium, chromium, lead, and mercury.[47] The LIBS setup was identical to the setup used for the mercury and oxygen studies.[46] The limits of detection were also found as a function of delay time and gate width. At the optimal gate width for all the elements, the limits of detection ranged from 10 μg/m^3 to 400 μg/m^3. With only one detector, finding a gate width and delay time that is suitable for all elements was necessary. A delay time of 12 μs and gate width of 4 μs gave detection limits near the optimal for As, Be, Cd, and Hg; however, much lower limit of detections were obtained for Pb, and Cr at a later delay time of 50 μs and a gate width of 150 μs.

The conditional analysis algorithm was later implemented for the analysis of ambient air particles.[48] A PM 10 inlet, an inlet collecting all particles smaller than 10 μm, was connected to the LIBS system via a transfer line and the aerosol chamber was kept 1 torr below atmospheric pressure to sample the ambient aerosols. Aluminum, magnesium, calcium, sodium were monitored before and after the Fourth of July. Concentrations of magnesium and aluminum increased over the holiday while calcium and sodium did not. Low analyte mass detection limits for the various elements were obtained: sodium 3.3 fg, magnesium 1.2 fg , and calcium 0.5 fg.

A systematic study of the precision in single shot analysis and factors influencing it was also conducted on this same system.[49] Prior to the study of shot to shot precision an investigation of breakdown thresholds was necessary. At laser pulse irradiances around the breakdown threshold, erratic behavior in the emission signal was observed so variation in the peak to base is also high. The breakdown threshold, defined as the laser energy corresponding to the plasma forming 90% of the time, in clean air and nitrogen was determined to be 160 to 170 mJ/pulse. Addition of water droplets or solid titanium and sodium particles, generated by nebulization of atomic absorption standards, reduced the breakdown threshold, but for the entire study, laser pulse energies greater than 180 mJ/pulse were used to insure that the frequency of breakdown was 100%.

Deposition of energy into the air plasma reached the maximum value of 60 % at 255 mJ pulse energy. This agreed well with the expected value for percent absorption when spherical aberration was taken into account. To examine the effects of laser pulse energy on the precision of peak to base measurements, the emission signal for the carbon neutral atomic transition at 247.856 nm was used because air was a homogenous and constant source for carbon. In order to only see effects due to the laser pulse energy, the peak to base values for carbon were obtained from spectra, which were taken at the optimum delay time for that particular pulse energy. The peak to base value increased as the laser pulse energy increased, however, the relative standard deviation (RSD) decreased to the same value for pulse energies greater than 275 mJ/pulse.

Using the same delay times that gave optimal carbon signals at the various pulse energies, the plasma temperatures were measured by seeding the air with iron particles and using the iron ion emission lines to construct Boltzmann plots. The plasma temperatures were again found to be roughly the same regardless of laser pulse energy. This confirmed that optimization of delay time was actually optimizing the plasma temperature. Decreased spatial variability at laser powers above the value at which the maximum percentage of laser energy was absorbed was deemed to be the reason for the lower RSDs at these higher laser powers.

Orthopaedic debris particles, due to the wearing of an implanted hip or knee prosthetic, were also detected with this same system.[50] Here the cobalt-chromium particles, generated either from synovial fluid samples or from an alloy which was made into a stock solution, were analyzed. A delay time of 40 μs and a gate width of 20 μs were found to be the optimal conditions for analysis using the Cr(I) lines of 359.35 nm and 360.53 nm and the Co(I) lines of 340.51 nm and 345.45 nm. The solutions were diluted so that single particle analysis could be performed. Size distributions of the wear debris particles were constructed for the 2 component particles by first finding the equivalent mass concentration from the emission signal and the corresponding calibration curve and then using this mass concentration and the plasma volume to obtain the mass of the particles. This relationship is illustrated by the following equation:

$$x = \frac{(m_a)}{V_{Plasma}} \qquad [7]$$

here x is the equivalent mass concentration in μg/cm^3 and V_{Plasma} is the volume of the plasma cm^3. This mass of the analytes m_a in μg, can be substituted into the following equation to obtain the equivalent spherical diameter , D in cm, of the particles:

$$D = \left[\frac{6(mass_{cobalt} + mass_{chromium})}{\pi \rho} \right]^{1/3} \qquad [8]$$

here the density, ρ in g/cm^3, was taken to be density for the bulk alloy. Ratios of the masses of cobalt and chromium in the individual particles for all samples were also found giving more insight to the cause of the wear of these implants. The generated size distributions ranged from 200 to 800 nm with a mean diameter of 385 nm and compared well with previous measurements done with visible light spectroscopy and scanning electron microscopy.

Plasma volume measurements are critical in the above algorithm and the exact definition of this volume was further explored.[51] The plasma volume was defined in three different ways the first of which was the statistical plasma volume, V_S. This statistical plasma volume, V_S, cm^3, was the volume for a set particle sampling frequency, F, and a set number density, N in units of cm^{-3}. The equation below illustrates the relationship between these variables and the statistical plasma volume.[51]

$$V_S = -\frac{\ln(1-F)}{N} \qquad [9]$$

An additional plasma volume was also defined in terms of the emission signal. This definition could only be used when the particle sampling rate was low, which is typical for many applications in aerosol analysis. In this case the sampling frequency F, was approximately equal to number density of the aerosol, N in cm^{-3}, times the sampling volume, V_e in cm^3 as shown in the following equation.

$$F = N \times V_e \qquad [10]$$

The expression for actual mass concentration, C in μg/cm^3, was equal to the product of mean aerosol analyte mass, $\overline{m}$ in μg, and the number density of the aerosol, N in cm^3, and this was shown by the following equation.

$$C = \overline{m} \times N \qquad [11]$$

The conditional analysis algorithm also yielded another relationship between the actual mass concentration, C in μg/cm^3, and the equivalent mass concentration found from the ensemble averaged particle spectra, X in μg/cm^3 and this was shown in the equation below, where again F was the particle sampling rate.

$$C = X\ F \qquad [12]$$

When equations 10 and 11 were substituted into equation 12 the following important equation was derived:

$$\overline{m}\ N = X\ N\ V_e \qquad [13]$$

This equation gave the volume that was determined via the LIBS signal from the analyte elements and was termed the emission volume, V_e.

The physical volume of the plasma, that is the volume of the plasma as determined by measurements of the optical density, was directly measured using transmission measurements while the statistical plasma volume was measured using aerosols containing monodispere particles with a known number density. The emission volume was measured using monodisperse aerosols with various particle sizes. The statistical volume, 1.17 mm^3, was smaller than the physical volume, 1.44 mm^3, which was also smaller than the emission volume, 2.38 mm^3.

Intensified charge coupled devices (iCCD) or intensified photodiode arrays (iPDA) are typically used in aerosol analysis. The need for more portable detectors that are inexpensive has motivated the assessment of non-intensified charge coupled devices (CCD) for aerosol analysis.[52] A study was conducted comparing a CCD to an iCCD detector for the analysis of calcium aerosols. To insure proper comparison the linear dispersion of the two detectors was matched. The signal to noise ratios at various delay times for the ensemble averaged spectra were found to be much greater for the iCCD system and the signal to noise ratios for the averaged single shot spectra were found to be larger especially at the later delay times. As stated previously the ratio of the peak intensity to the base continuum was used during quantitative analysis of aerosols. This leads to the largest disadvantage of the CCD detector; its inability to measure continuum emission at late delay times when the signal to noise of the emission line is significantly better. The authors concluded that the detector was useful in many applications but would not be suitable for quantitative analysis of aerosols.

Agglomerates of *Bacillus globigi* spore particles were most recently detected using a LIBS system with a pulsed Q-switched Nd:YAG operating at the second harmonic of 532 nm, and at a pulse energy of 200 mJ.[53] For different spore agglomerates of *B. globigi* large signals were measured for Mg, Ca, and Na.[53]

In the last decade many significant advances in LIBS analysis of gases and aerosols have been seen. Fundamental work has also given a more detailed process of the LIBS plasma in terms of its evolution and has also further determined parameters that affect analytical work such as electron density and excitation temperature. Analysis of aerosols by LIBS is now well developed and is being directed towards the analysis of bioaerosols.

CHAPTER 3

CURVE OF GROWTH METHODOLOGY APPLIED TO LASER INDUCED BREADKDOWN SPECTROSCOPY PLASMAS OF GASES

Introduction

The curve of growth (COG) is a useful tool in laser induced breakdown spectroscopy (LIBS).[54] It gives insight not only into the upper limit of linear calibration, but also into the relative contributions of Doppler and Lorentzian broadening in the plasma. Additional plasma parameters such as collisional cross sections may be determined if other parameters, such as plasma temperature, are known. Characterization of particle containing plasmas may also be possible using curve of growth theory. Yalcin and coworkers determined that the number density of electrons and the excitation temperature in the plasma were not significantly different for a nitrogen plasma and a nitrogen plasma containing approximately 100 $MgCl_2$ particles.[26] It then may be possible to characterize a particle containing plasma by examining a pure gas plasma.

The curve of growth is roughly generated by plotting the log of the peak area versus log of the number density of the analyte atoms. Appearance of non-linearity in these curves is a result of atoms in the ground state, for resonance transitions, or atoms in the lower state, for non-resonance transitions, absorbing radiation emitted by atoms in the excited state. This effect is termed self absorption. Curve of growth theory is frequently applied to absorption measurements of gases such as hydrogen, carbon dioxide, and argon in the field of astrophysics, where hydrogen is present in high concentrations in stars,[55] carbon dioxide produces carbon monoxide in the unstable atmosphere of Mars,[56] and argon is present in large concentrations in the lunar atmosphere.[57] When applied to emission measurements obtained from LIBS plasmas, information on line broadening may be gained, evolution of the plasma over time may be further ascertained and the presence of local thermodynamic equilibrium may be further explored. In this work, the applicability of curve of growth theory to LIBS plasmas of gaseous samples is tested and the broadening processes in gas plasmas are examined.

Background

The non –linearity in curves of growth in absorption measurements was first seen experimentally by Ladenburg and Reiche in 1910 using resonance vapor lamps as light sources and absorption cells[58] and the theory behind this curvature was discussed early on by Mitchell and Zemansky in 1934.[59] The methodology was applied to flame spectroscopy but also further expanded upon by Hinnov [60] and others [61-63]. Theoretical and experimental considerations were summarized by Alkemade and Hollander.[64] The shape of these curves in absorption, emission, and fluorescence flame spectroscopy and characterization of this shape under conditions of a line or continuum excitation source were also discussed in detail by Zeegers and coworkers.[65] This work was further expanded upon to determine the absolute atomic number density in a flame from a fluorescence COG.[66] Determination of collisional cross sections via classical COG theory was first done by Hinnov[60,67] and was later repeated by combining classical and semi-classical theory, where classical theory and Maxwell equations are also used to treat the radiation; however, quantum mechanics was used to describe the atoms.[68] Broadening parameters for several neutral carbon lines for a plasma formed by an arc were also evaluated.[69]

The curve of growth method was first applied to the LIBS plasma by Gornushkin, *et al*[54] where steel standards with varying concentrations of chromium were used to generate experimental curves of growth using the chromium resonance line at 425 nm. These resulting curves were compared to theoretical curves, allowing the damping or *a*-parameter to be determined as well as the number density of ground state chromium atoms that corresponded to the transition from an optically thin to an optically thick plasma. The *a*-parameter indicated the relative amount of Lorentzian and Doppler broadening in the plasma. The *a*-parameters, when extrapolated to lower temperatures seen in flames, using the formula developed by Alkemade, *et al*[64], $a \propto T^{-1.2}$, agreed well with typical values seen for chromium. This proved that at longer delay times, where LTE is established, COG theory was indeed valid. The collisional cross section of the chromium atom with the nitrogen gas molecule was also estimated.

COG theory was later applied by Aragon, *et al*[70] to determine the *a*-parameter for seven self absorbed Fe(I) spectral lines in Fe-Ni alloys and the number density of Fe atoms in a 100% Fe sample was found to be 7.3×10^{15} cm^{-3}. Inhomogeneity of the plasma over both space and time was shown to affect the validity of the theory of COG. Aguilera and coworkers[71] developed a two spatial region model that attempted to correct for the inconsistencies between the theoretical and experimental curves in earlier times in the plasma, which in these experiments, were 4-5 μs; however, the single region model was found to be acceptable at later delay times of 15-18 μs where the plasma became more homogeneous due to cessation of plasma expansion and the continued plasma cooling.

The concept of self absorption was also introduced into the calibration-free LIBS algorithm[72] and a simplified approach to account for self absorption was also introduced into a calibration method used to determine the elemental composition of soils and Antarctic marine sediments.[73]

Theory

The integral absorption, A_t (Hz), which is the integral of the absorption coefficient over the frequency profile of the line, is derived from Beer's Law and is expressed as follows:

$$A_t = \int_{line} \left[1 - e^{(-k(\nu)l)}\right] d\nu \qquad [1]$$

where k(v) is the frequency-dependent absorption coefficient (cm^{-1}), and *l* is the absorption path length (cm). In LIBS the curve of growth results from plasma emission, I_ν, expressed here in W m^{-2} sr^{-1}, and this can be related to absorption by the following equation through the blackbody spectral radiance at the line center, $B^b_{\nu m}$(W m^2 sr^{-1} Hz^{-1}):[18]

$$I_\nu = B^b_{\nu m}\, A_t = \frac{2h\nu^3}{c^2} \frac{1}{e^{\frac{h\nu}{kT}} - 1} A_t \qquad [2]$$

where *h* is the Planck constant (J s), *c* is the speed of light (m s^{-1}), v is the frequency of the transition of interest (Hz), *k* is Boltzmann's constant (JK^{-1}), and *T* is plasma temperature (K).

The frequency-dependent absorption coefficient, *k(v)*, is expressed by the following:[74,61]

$$k(\nu) = k_0 \frac{a}{\pi} \int_{-\infty}^{\infty} \frac{e^{-t^2} dt}{(t - x)^2 + a^2} \qquad [3]$$

where k_0, a, and x are described in the following equations:

$$k_0 = 2\pi^{\frac{3}{2}} \frac{e^2}{m_e c} \frac{n_0 f}{b} \qquad [4]$$

$$b = \frac{\pi \Delta \nu_D}{\sqrt{\ln 2}} \qquad [5]$$

$$a = \frac{\Delta \nu_L}{\Delta \nu_D} \sqrt{\ln 2} \qquad [6]$$

$$x = \frac{2(\nu - \nu_0)}{\Delta \nu_D} \sqrt{\ln 2} \qquad [7]$$

here e is the elementary charge (C), m_e is the mass of the electron (kg), n_0 is the number density of the analyte atoms, f is the transition oscillator strength (dimensionless), ν_0 is the central frequency of line (Hz), and $\Delta\nu_N$, $\Delta\nu_L$, and $\Delta\nu_D$ is the natural, Lorentzian, and Doppler line half-widths. The frequency-dependent absorption coefficient, $k(\nu)$, is comprised of the Voigt line profile function.

In a LIBS plasma the important broadening mechanisms are Doppler, and Lorentzian. Lorentzian broadening is a convolution of natural broadening, Stark broadening, resonance broadening, and van der Waals broadening.[18]

Doppler broadening, broadening due to the emitting atoms moving at different velocities relative to the incoming photons, $\Delta\nu_D$, is the simplest broadening due to its dependence only on plasma temperature, T, (K), the mass of the emitting atom, m, (kg), and the frequency of the transition of interest, ν_0, (Hz).

$$\Delta \nu_D = \frac{\nu_0}{c} \left(\frac{8\pi k T}{m} \right)^{1/2} \sqrt{\ln 2} \qquad [8]$$

This broadening mechanism is typically small in comparison to the Lorentzian broadening for LIBS plasmas formed under atmospheric pressure and LIBS plasmas that are no longer optically thin because the high electron number density in the plasma dictates a primarily Stark broadened emission lines from the plasma.[18]

Stark broadening often plays an important role in contributing to the overall line broadening especially at early delay times in the plasma when the number density of electrons is very high. Perturbation of atoms by an electric field, which arises from the ions and electrons present in the plasma, cause lines to shift as well as broaden.[75] For all atoms except for hydrogen, this interaction is quadratic meaning the interaction is inversely proportional to the fourth power of the distance, r, from the perturber to the atom , as shown by the relationship,$\sim 1/r^4$, and it is also proportional to the electric field strength, E, by $\sim E^2$.

Griem[74] has calculated the electron impact half width w (m), the shift to width ratio d/w (dimensionless), and the ion broadening parameter α (dimensionless), for an electron number density, n_e, of 10^{16} cm^{-3} at various plasma temperatures T (K). These values were calculated using the impact approximation including quasi static line broadening due to the ions in the plasma. The shift due to the Stark effect, $\Delta\lambda_{Stark\ shift}$, and broadening due to the stark effect $\Delta\lambda_{Stark\ width}$ are expressed in the following equations with the electron number density in m^{-3}:

$$\Delta\lambda_{Stark\ shift} = \left[\frac{d}{w} + 6.32\times10^{-6}\, n_e^{\frac{1}{4}}\,\alpha\times\left(1-0.0068 n_e^{\frac{1}{6}} T^{-\frac{1}{2}}\right)\right]\times10^{-22}\, w n_e \qquad [9]$$

$$\Delta\lambda_{Stark\ width} = 2\left[1 + 5.53\times10^{-6}\, n_e^{\frac{1}{4}}\,\alpha\times\left(1-0.0068 n_e^{\frac{1}{6}} T^{-\frac{1}{2}}\right)\right]\times10^{-22}\, w n_e \qquad [10]$$

Resonance broadening is a result of the interaction of the emitting atoms of interest with atoms of the same kind in the ground state. These interactions are classified as dipole-dipole but an approximate formula has only been developed for resonance transitions.[76]

The final type of broadening, Van der Waals broadening, is due to the interaction of two atoms of a different kind, one of which is the radiating atom which has an oscillating dipole that produces a dipole in the perturbing atom. This interaction can be either adiabatic or diabatic. The diabatic interaction will cause the atom to change excited levels altering the lifetime of the transition; however, the adiabatic, which is more common, changes the phase of the emitted radiation. These two processes result in shifting of the line which is represented by, $\Delta\lambda_{Vander\ Shift}$. and broadening the line, which is represented by, $\Delta\lambda_{Vander\ width}$,. The magnitude of these effects is dependent upon the relative velocity of the atoms υ (m/s), the number density of the perturbing atoms n_{pert} (m^{-3}), and the interaction potential constant C_6 (m^6s^{-1}) and is shown in the following equations.[18]

$$\Delta\lambda_{Vander\ Shift} = 0.98 C_6^{\frac{2}{5}} \upsilon^{\frac{3}{5}} n_{pert} \frac{\lambda^2}{c} \qquad [11]$$

$$\Delta\lambda_{Vander\ width} = 2.71 C_6^{\frac{2}{5}} \upsilon^{\frac{3}{5}} n_{pert} \frac{\lambda^2}{c} \qquad [12]$$

Numerous souces of Lorentzian broadening restrict the *a- parameter* to only being an indicator of the ratio of all of the Lorentzain broadening components to the Doppler component. The shape of the double logarithmic plot of $A_t/2b$ versus n_0fl/b, the theoretical curve of growth, dictates the value of this *a-parameter* and the n_0fl quantity can be determined via the curve fitting process. A sample of these curves is shown in Figure 3-1.[18]

This means that the absorption path length can be determined if the oscillator strength is known. Additionally the intersection of the extrapolated lines from the linear region, slope equals 1, and non-linear region, slope equals ½, yields the transition from an optically thin to optically thick plasma and the value for the product of the number density of the analyte atoms, the oscillator strength, and the optical pathlength.[77] Many other plasma parameters such as plasma temperature and collisional cross sections may be found using this ratio but usually require prior knowledge of the type of broadening processes in the plasma. To determine an unknown collisional cross section the plasma temperature must be determined using another method. As seen in equation 2, the integral absorption, A_t, is related to the emission by a constant factor. Calibration plots of the emission peak area for the analyte transition versus the number density of the analyte atoms are converted to log –log plots before fitting to the absorption curves of growth, seen in Figure 3-1.

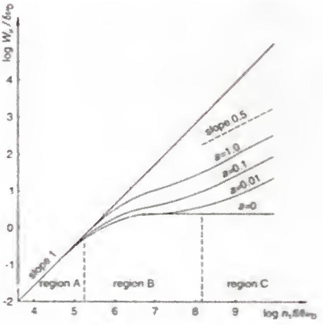

Figure 3-1: Theoretical curves of growth.[18]

The curve of growth model is constructed under the following assumptions:

1. For all points of the curve the plasma is assumed to be isothermal, meaning spatial and temporal temperature gradients in the plasma are absent.
2. Local Thermodynamic Equilibrium (LTE) exists at the times used to generate these curves.
3. The plasma is homogenous and spherical in shape possessing a path length of *l*.

Experimental

Instrument setup

The LIBS setup, shown in Figure 3-2, consisted of a pulsed Nd:YAG laser (Quantel Brilliant, France),operating at fundamental wavelength of 1064 nm and at a repetition rate of 5 Hz with a pulse width of 5 ns. This pulsed radiation was focused through a biconvex lens (37.5 mm focal length, 25 mm diameter) to form a plasma in a chamber containing the gases of interest. The resulting plasma emission was collected at a 90° angle from the axis of plasma formation by a plano-convex lens (75mm focal length, 50 mm diameter). The lens was placed at twice its focal length from the plasma and the slit so that the plasma was imaged onto the slit of the spectrometer. The 0.5-m focal length spectrometer (SpectroPro-500i, Acton Research Corporation, Acton, Massachusetts) with a 1200, 2400, 3600 grooves/mm grating collected and dispersed the plasma emission onto the gated intensified Charge Coupled Device (iCCD) (ST-138S, PG200, ITE/CCD-576, Princeton Instruments, Trenton, New Jersey). This instrumentation allowed for plasma emission to be collected at various times in the plasma evolution.

The resolution was 0.05 nm for the 2400 g/mm grating and 0.03 nm for the 3600 g/mm for the chosen slit width of 10 μm. Plasma lifetime measurements were measured with a side-on photomultiplier tube, PMT, (Hamamtsu, Japan , R446). To prevent the excess laser radiation from entering the PMT a cold mirror, which reflected all radiation below 700 nm and transmitted any excess 1064 nm, was placed at a 45 degree angle to direct light from the plasma to the PMT which was terminated into a 100 MHz oscilloscope (Techtronix, TDS 3012,Beaverton, Oregon). The same collimating lens as used in the emission measurements, focused plasma radiation onto the cold mirror. A schematic of this setup is shown in Figure 3-3. Calibrated neutral density filters were used throughout peak area measurements, Boltzmann temperature determinations, and plasma lifetime measurements. The laser pulse energy measurements were obtained with a calorimeter power meter (Scientech, Astral Series calorimeter AC5001, S310 digital readout, Boulder Colorado).

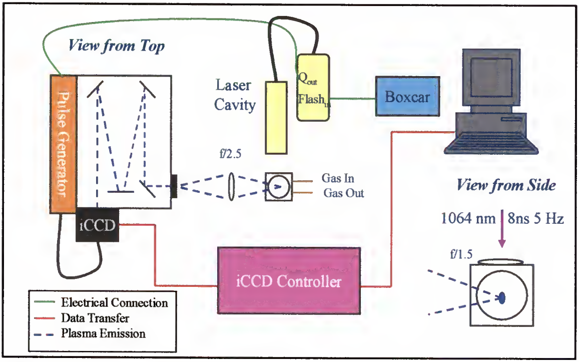

Figure 3-2: Schematic of LIBS instrument setup.

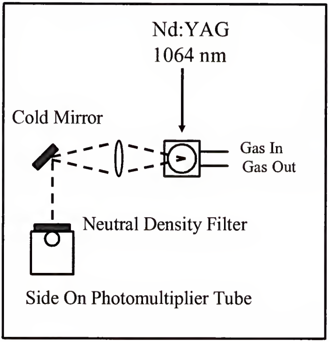

Figure 3-3: Schematic for plasma lifetime measurements.

Gas Introduction and Mixing System

The gas introduction and mixing system was static with the two gases being introduced via needle valves into a closed off stainless steel mixing vessel. The pressure gauge (Wallace and Tiernan, Model FA 160, Belleville, New Jersey) resided upstream from the mixing vessel. The gases were added in the desired percent by pressure until a total pressure of 755 torr was reached. Once the gases were thoroughly mixed they were released to the chamber where the pressure measured upstream decreased to 720 torr due to the increase in the volume the gases were occupying. Before the gases were introduced into the chamber, the chamber was pumped down to 300 mtorr by means of a diffusion pump (BOC Edwards, Model RV 12, England). The entire system, including the mixing vessel and the gas lines leading to the vessel, was pumped down to 700 mtorr with the same pump before filling the mixing vessel. A schematic of the gas introduction system is shown in Figure 3-4. The gases were introduced slowly to avoid any temperature changes in the vessel, added in a sandwich fashion to facilitate proper mixing, and allowed necessary mixing time.[78]

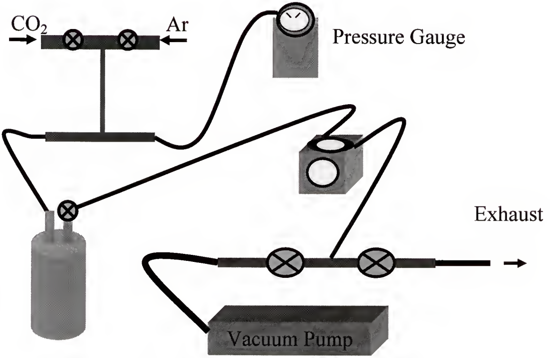

Figure 3-4: Schematic of Gas Introduction and Mixing System

Analyte and Mixing Gas Selection

In order to obtain a curve of growth, a region of the calibration curve for the analyte of interest must be optically thick. It is known if the product of the absorption coefficient, $k(\lambda)$ in cm^{-1} and the optical path length, l in cm, is much greater than one, then the plasma is optically thick. The absorption coefficient was determined from the absorption cross section $\sigma(\lambda)$ (cm^{-2}), and the atomic number density for the lower state n_i (cm^{-3}).[77]

$$\sigma(\lambda) = \frac{k(\lambda)}{n_i} \qquad [13]$$

Optical cross sections, $\sigma(\lambda)$,were determined by the following formula:

$$\sigma(\lambda) = 8.917 \times 10^{-13} f_{ij} \lambda^2 \; S(\lambda) \qquad [14]$$

where f_{ij} is the oscillator strength, λ is the transition wavelength in cm, $S(\lambda)$ is the spectral profile function in cm^{-1}, and the constant is in units of cm. The analyte gas was chosen prior to fitting of the experimental curves, therefore an estimation of the spectral profile function was necessary. The spectral function was estimated by placing a rectangle around the approximate line profile, the height of which is the maximum absorption coefficient and the width of which is the spectral line kernel, $\Delta\lambda_{eff}$, which was defined as the region within the full width at half maximum of the spectral line. A diagram of these parameters is shown in Figure 3-5.

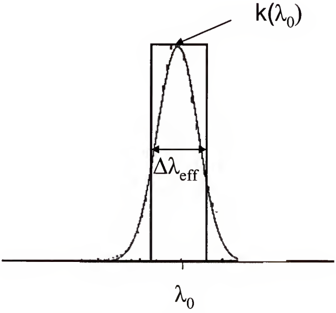

Figure 3-5: A diagram of the spectral line profile.

This relationship between the spectral profile function and the spectral line kernel is summarized by the following:

$$S(\lambda_0) = \frac{k(\lambda_0)}{\int k(\lambda)d\lambda} = \frac{1}{\Delta\lambda_{eff}} \qquad [15]$$

where $k(\lambda_0)$ is the maximum absorption coefficient and the integral of $k(\lambda)d\lambda$ is the area under the absorption profile and is always normalized to 1. The width of the spectral line kernel was assumed to be 0.02 nm based on previous line profiles in LIBS.[54] The absorption path length, l, was assumed to be 0.0526 cm and the number density of lower state atoms, n_i, was determined for a ground state analyte atom number density of 9.73 10^{18} cm^{-3} using the Boltzmann equation. Transitions of atoms of inert gases were examined and all resonance transitions were found to be in the far UV region.

Table 3-1: Values of $\sigma n_i l$ for various possible analyte transitions.

Analyte Atom	*Transition λ, nm*[79]	*$\sigma n_i l$ (dimensionless)*
Ar	852.1441	0.1092
Ar	811.5311	0.2957
C	193.0905	3647
C	247.8561	375

The best choice of analyte gas, as indicated by the $\sigma n_i l$ in Table 3-1, was a gas containing carbon and the most inexpensive and least toxic of carbon containing gases was carbon dioxide, CO_2.

The selection of mixing gas was critical for the following reasons: the gas must mix well with the analyte gas, it must be inert, and it should also provide transitions that may be used for Boltzmann temperature determinations. In plasma characterization, temperatures allow the amount of Doppler broadening and the line profile type to be determined. The atomic species of carbon dioxide lack the number of necessary, self absorption free, spectral transitions needed for a Boltzmann determination, meaning the mix gas should provide the transitions.

Two inert gases, argon and nitrogen, were investigated further. The first criterion to evaluate for these gases was their ability to mix with CO_2. A good indicator of if the gases will mix sufficiently is the interdiffusion coefficients, which are related to the atomic weights of the two gases. It thus follows that argon would form a homogenous mixture with carbon dioxide before nitrogen because they are similar in molecular weight but both gases would mix rapidly with the CO_2.[78]

Temperature measurements of inductively coupled plasmas, ICPs, using relative intensities of neutral or ionic transitions of argon are frequently performed using Boltzmann plots.[80] Boltzmann temperature determinations were also successfully performed on LIBS plasmas in low temperature plasmas using nitrogen ion lines.[81] Either gas would be suitable for Boltzmann temperature measurements in LIBS, however the argon lines can easily be used to determine plasma temperatures at later times in the plasma because they are neutral lines, while nitrogen ion lines may not be seen at later delay times. Argon was then chosen as the mixing gas for carbon dioxide.

Results and Discussion

Calibration plots were constructed for partial pressures of carbon dioxide ranging from 0 to 755 torr using the peak area of the non-resonance 193.059 nm, and 247.856 C(I) transitions. These pressures corresponded to between 0 and 2.315×10^{19} atoms of carbon per cubic centimeter. Plots were obtained for two different laser pulse energies of 68 and 148 mJ/pulse and for delay times of 0.5, 2, 5, 7 and 9 μs for each pulse energy. A gate width of 0.1 μs was utilized for calibration and Boltzmann measurements. For the duration of this gate, plasma parameters, including temperature, were approximately constant. The calibration plots corresponding to laser pulse energies of 68 and 148 mJ/pulse are shown in Figures 3-6- 3-15 for the 193.059 nm transition and 3-16-3-25 for the 247.856 nm transitions, respectively. The 3600 grooves/mm grating was chosen for peak area measurements, while the 2400 grooves/mm grating was chosen for the Boltzmann plot measurements.

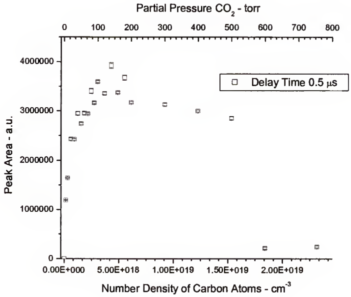

Figure 3-6: Calibration plot of peak area versus carbon concentration, expressed either as partial pressure of CO_2 or number density of carbon atoms, for the 193.0905 nm transition and the following instrumental conditions: a laser pulse energy 68 mJ/pulse and a delay time 0.5 μs and gate width 0.1 μs on the gated iCCD.

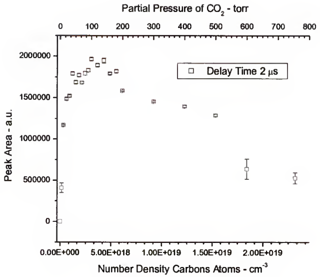

Figure 3-7: Calibration plot of peak area versus carbon concentration, expressed either as partial pressure of CO_2 or number density of carbon atoms, for the 193.0905 nm transition and the following instrumental conditions: a laser pulse energy 68 mJ/pulse and a delay time 2 µs and gate width 0.1 µs on the gated iCCD.

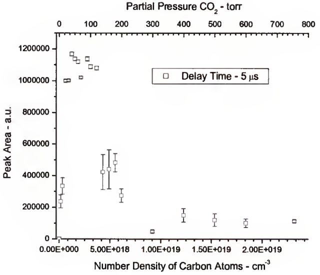

Figure 3-8: Calibration plot of peak area versus carbon concentration, expressed either as partial pressure of CO_2 or number density of carbon atoms, for the 193.0905 nm transition and the following instrumental conditions: a laser pulse energy 68 mJ/pulse and a delay time 5 µs and gate width 0.1 µs on the gated iCCD.

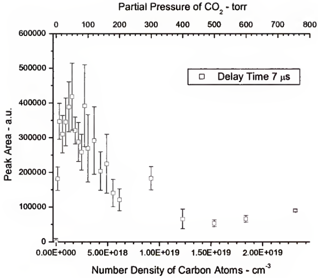

Figure 3-9: Calibration plot of peak area versus carbon concentration, expressed either as partial pressure of CO_2 or number density of carbon atoms, for the 193.0905 nm transition and the following instrumental conditions: a laser pulse energy 68 mJ/pulse and a delay time 7 μs and gate width 0.1 μs on the gated iCCD.

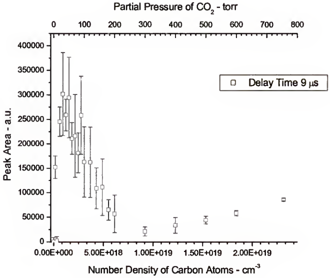

Figure 3-10: Calibration plot of peak area versus carbon concentration, expressed either as partial pressure of CO_2 or number density of carbon atoms, for the 193.0905 nm transition and the following instrumental conditions: a laser pulse energy 68 mJ/pulse and a delay time 9 μs and gate width 0.1 μs on the gated iCCD.

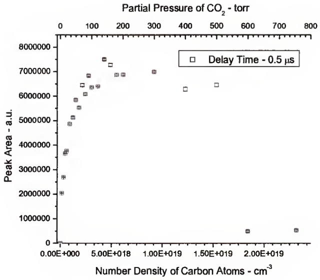

Figure 3-11: Calibration plot of peak area versus carbon concentration, expressed either as partial pressure of CO_2 or number density of carbon atoms, for the 193.0905 nm transition and the following instrumental conditions: a laser pulse energy 148 mJ/pulse and a delay time 0.5 μs and gate width 0.1 μs on the gated iCCD.

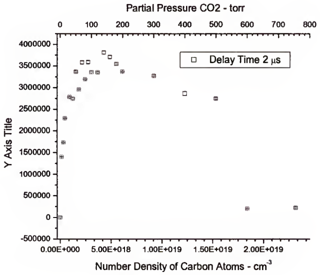

Figure 3-12: Calibration plot of peak area versus carbon concentration, expressed either as partial pressure of CO_2 or number density of carbon atoms, for the 193.0905 nm transition and the following instrumental conditions: a laser pulse energy 148 mJ/pulse and a delay time 2 μs and gate width 0.1 μs on the gated iCCD.

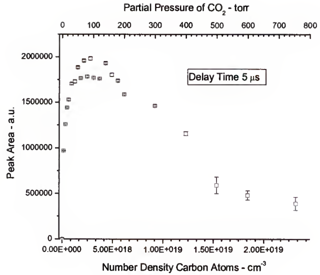

Figure 3-13: Calibration plot of peak area versus carbon concentration, expressed either as partial pressure of CO_2 or number density of carbon atoms, for the 193.0905 nm transition and the following instrumental conditions: a laser pulse energy 148 mJ/pulse and a delay time 5 μs and gate width 0.1 μs on the gated iCCD.

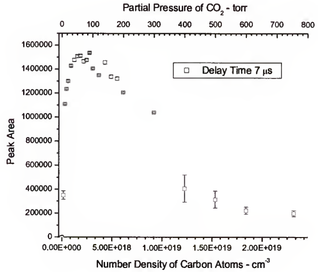

Figure 3-14: Calibration plot of peak area versus carbon concentration, expressed either as partial pressure of CO_2 or number density of carbon atoms, for the 193.0905 nm transition and the following instrumental conditions: a laser pulse energy 148 mJ/pulse and a delay time 7 μs and gate width 0.1 μs on the gated iCCD.

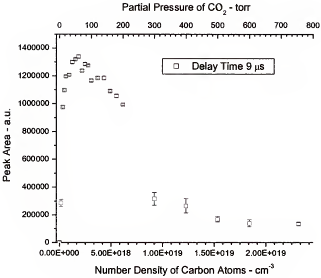

Figure 3-15: Calibration plot of peak area versus carbon concentration, expressed either as partial pressure of CO_2 or number density of carbon atoms, for the 193.0905 nm transition and the following instrumental conditions: a laser pulse energy 148 mJ/pulse and a delay time 0.5 µs and gate width 0.1 µs on the gated iCCD.

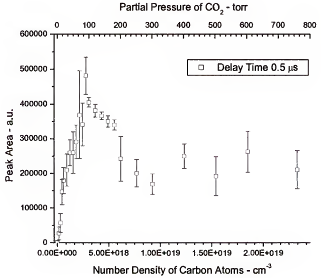

Figure 3-16: Calibration plot of peak area versus carbon concentration, expressed either as partial pressure of CO_2 or number density of carbon atoms, for the 247.8561 nm transition and the following instrumental conditions: a laser pulse energy 68 mJ/pulse and a delay time 0.5 µs and gate width 0.1 µs on the gated iCCD.

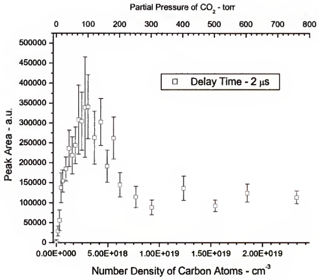

Figure 3-17: Calibration plot of peak area versus carbon concentration, expressed either as partial pressure of CO_2 or number density of carbon atoms, for the 247.8561 nm transition and the following instrumental conditions: a laser pulse energy 68 mJ/pulse and a delay time 2 μs and gate width 0.1 μs on the gated iCCD.

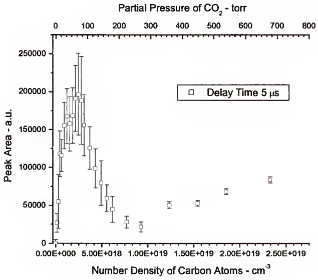

Figure 3-18: Calibration plot of peak area versus carbon concentration, expressed either as partial pressure of CO_2 or number density of carbon atoms, for the 247.8561 nm transition and the following instrumental conditions: a laser pulse energy 68 mJ/pulse and a delay time 5 μs and gate width 0.1 μs on the gated iCCD.

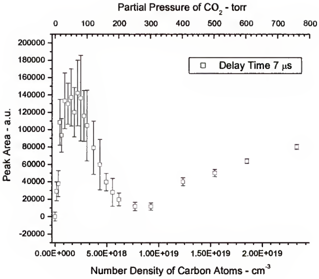

Figure 3-19: Calibration plot of peak area versus carbon concentration, expressed either as partial pressure of CO_2 or number density of carbon atoms, for the 247.8561 nm transition and the following instrumental conditions: a laser pulse energy 68 mJ/pulse and a delay time 7 μs and gate width 0.1 μs on the gated iCCD.

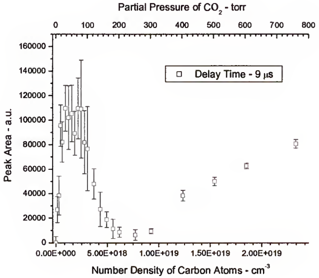

Figure 3-20: Calibration plot of peak area versus carbon concentration, expressed either as partial pressure of CO_2 or number density of carbon atoms, for the 247.8561 nm transition and the following instrumental conditions: a laser pulse energy 68 mJ/pulse and a delay time 9 μs and gate width 0.1 μs on the gated iCCD.

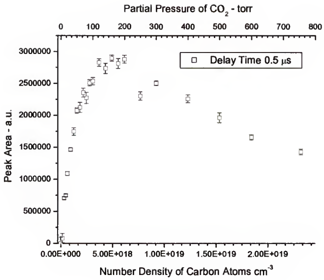

Figure 3-21: Calibration plot of peak area versus carbon concentration, expressed either as partial pressure of CO_2 or number density of carbon atoms, for the 247.8561 nm transition and the following instrumental conditions: a laser pulse energy 148 mJ/pulse and a delay time 0.5 μs and gate width 0.1 μs on the gated iCCD.

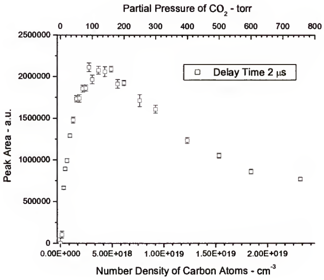

Figure 3-22: Calibration plot of peak area versus carbon concentration, expressed either as partial pressure of CO_2 or number density of carbon atoms, for the 247.8561 nm transition and the following instrumental conditions: a laser pulse energy 148 mJ/pulse and a delay time 2 μs and gate width 0.1 μs on the gated iCCD.

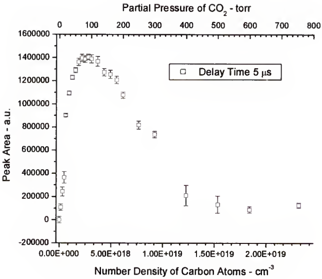

Figure 3-23: Calibration plot of peak area versus carbon concentration, expressed either as partial pressure of CO_2 or number density of carbon atoms, for the 247.8561 nm transition and the following instrumental conditions: a laser pulse energy 148 mJ/pulse and a delay time 5 μs and gate width 0.1 μs on the gated iCCD.

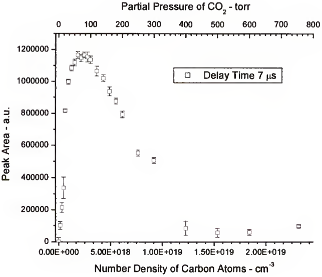

Figure 3-24: Calibration plot of peak area versus carbon concentration, expressed either as partial pressure of CO_2 or number density of carbon atoms, for the 247.8561 nm transition and the following instrumental conditions: a laser pulse energy 148 mJ/pulse and a delay time 7 μs and gate width 0.1 μs on the gated iCCD.

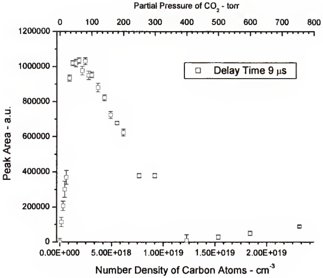

Figure 3-25: Calibration plot of peak area versus carbon concentration, expressed either as partial pressure of CO_2 or number density of carbon atoms, for the 247.8561 nm transition and the following instrumental conditions: a laser pulse energy 148 mJ/pulse and a delay time 9 μs and gate width 0.1 μs on the gated iCCD.

The calibration plots exhibited a decrease and this deviates from the traditional calibration plots which exhibit a change in slope in the log-log plot of the calibration data from 1 to ½ but still increase in intensity. The curves taken at the lower pulse energy curve over before those taken at the higher pulse energy; additionally, the earliest curvature is seen at the later delay times. This indicates a dependence on the plasma composition that was more pronounced at the later delay times.

Other more complex reasons for curvature could be the following: change in plasma composition which results in different plasma temperatures, and electron densities etc. along the calibration curve, analyte atoms in a cooler region of the plasma could absorb plasma emission, otherwise known as the postfilter effect, these atoms could also absorb this same emission and fluoresce, or the carbon dioxide could be dissociated incompletely in the plasma. A summary of these effects, the probability of their occurrence, and the ability to prove the effects experimentally are shown in Table 3-2.

Table 3-2: Possible explanations for non-self absorption curvature of calibration plots.

Explanation	Probability	Experimental
Plasma composition change – temperature and plasma lifetime	+++	Monitor continuum plasma lifetime and line broadening
Post Filter Effect	+-	Unable to make correction
Fluorescence	+-	Cannot prove experimentally
Incomplete dissociation of CO_2	+++	Monitor O (I) emission

Plasma lifetime measurements were taken for pure carbon dioxide and pure argon plasmas by observation of the decay in the plasma emission. This decay was measured with a photomultiplier tube (PMT) and a neutral density filter with an absorbance of 3 was placed in front of the PMT in order to obtain a linear response from the PMT. This filter filtered out the weaker line emission intensity leaving the PMT to measure continuum emission. The traces from the oscilloscope indicative of the plasma lifetime decay are shown in Figures 3-26 and 3-27.

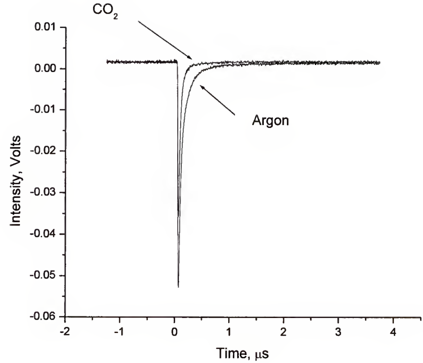

Figure 3-26: Oscilliscope trace of the plasma continuum as seen by the PMT for 68 mJ/pulse laser pulse energy.

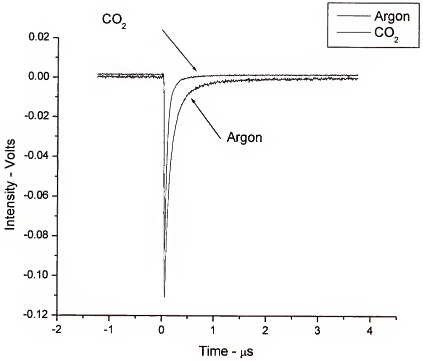

Figure 3-27: Oscilliscope trace of the plasma continuum as seen by the PMT for 148 mJ/pulse laser pulse energy.

It is apparent from the lifetime measurements that a pure carbon dioxide plasma has a shorter lifetime than a pure argon plasma. From these plasma continuum measurements, it was inferred that the plasma excitation temperature decayed faster for the pure carbon dioxide plasma because the plasma continuum reflects the temperature in the plasma.

Boltzmann temperature determinations of a carbon dioxide with 60 torr argon and a pure argon plasma were attempted using argon neutral and ion lines. Transitions used in these plots did not have a wide enough spread in their upper levels and or lacked transitions with energy levels in the middle of the spread. This resulted in extremely inaccurate temperature measurements. As stated previously, introduction of metal particles did not significantly change the plasma temperature, with Yalcin and coworkers[26] finding temperatures of 14800 +/- 100 K for pure nitrogen plasma and a nitrogen plasma containing 100 $MgCl_2$ particles. This allowed for the temperature of the two gases to be evaluated by introducing the pure gases as the nebulizing and coflow gas for generation of an iron aerosol using an iron atomic absorption standard (SPEX Certiprep, , 10,000 ppm). A pneumatic-type medical nebulizer (Hudson, model #1724) that was previously characterized by Hahn and coworkers was used to generate the iron aerosol.[82] The iron ion (Fe II) transitions, transition probabilities, and degeneracies and energies of their upper levels used for these plots are presented in Table 3-3. Sample spectra and a corresponding Boltzmann plot are shown in Figures 3-28, 3-29, and 3-30. The plasma temperatures obtained were not logical, ranging from 50000-90000 K, even with point left out such as the points circled in Figure 3-30. This may have been due to broadening of the lines, the lack of presence of local thermodynamic equilibrium and the inability to accurately calibrate the detector, which was necessary because the lines of interest were in different spectral windows.

Table 3-3: Parameters for Fe II transitions used to generate Boltzmann Plots.[79]

Wavelength, nm	Transition Probabiliy – s^{-1}	Degeneracy of Upper Level – dimens.	Energy of Upper Level – cm^{-1}
258.588	8.10×10^{7}	8	38660.04
259.94	2.20×10^{8}	10	38458.98
261.187	1.10×10^{8}	8	38660.04
261.762	4.40×10^{7}	6	38858.96
271.441	5.50×10^{7}	6	44784.76
272.754	8.50×10^{7}	4	45044.17
273.955	1.90×10^{8}	8	44446.88
275.574	2.10×10^{8}	10	44232.51
277.93	7.60×10^{7}	8	62322.43
278.369	7.00×10^{7}	10	62083.11

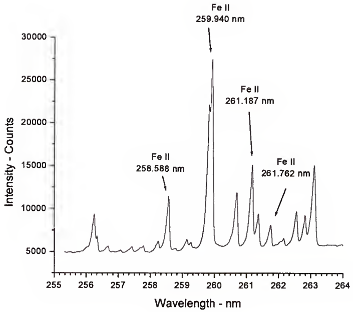

Figure 3-28: Ensemble averaged spectrum from first spectral window, for iron particles in argon gas, utilized in the Boltzmann Plot determination for the following instrumental conditions: laser pulse energy of 148 mJ/pulse, and a 5 μs delay, and 1 μs gate width on the iCCD.

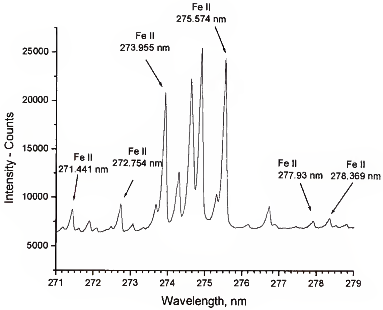

Figure 3-29: Ensemble averaged spectrum from second spectral window, for iron particles in argon gas, utilized in the Boltzmann Plot determination for the following instrumental conditions: laser pulse energy of 148 mJ/pulse, and a 5 μs delay, and 1 μs gate width on the iCCD.

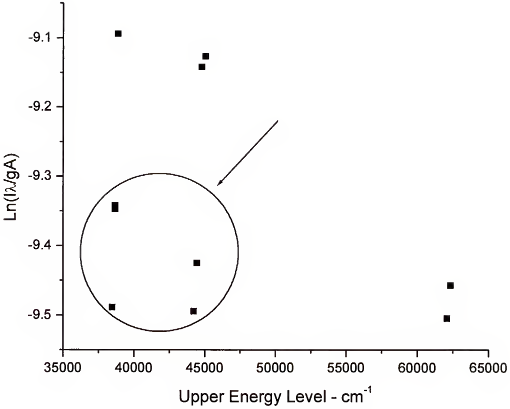

Figure 3-29: Boltzmann Plot of iron ion lines for the following instrumental conditions: laser pulse energy of 148 mJ/pulse, and a 5 μs delay, and 1 μs gate width on the iCCD. The points in circle were not included in the temperature determination.

Another indication of the conditions in the plasma conditions changing over the calibration curve is the continuum background. If the continuum background is indeed changing normalizing the peak area to the background continuum will correct for this effect. A comparison of a calibration plot constructed from peak to base values versus a calibration plot constructed from purely peak area values for the 193.0905 nm transition is shown in Figure 3-30.

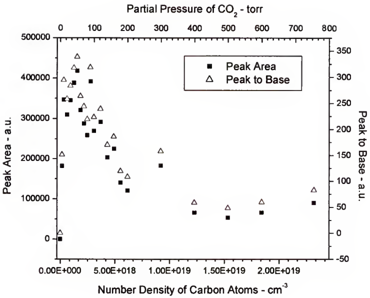

Figure 3-30: Calibration plots constructed from peak areas and peak to base values of the 193.0905 nm transition for instrumental conditions of a laser pulse energy 68 mJ/pulse and a delay time 7 μs and gate width 0.1 μs on the gated iCCD.

The normalization of the peak area to the continuum did not change the shape of the calibration plot indicating that the conditions in the plasma may not be changing drastically overall.

Examining the line width as a function of the delay time and the pressure of the analyte gas could also indicate changes in temperature, electron number density etc.. A simplified expression of the total line width, also called the Voigt width, was determined to be accurate to within 1 percent.[83] This equation relates the Voigt width, $\Delta\nu_{\text{Voigt}}$, to the Doppler and Lorentzian line width, $\Delta\nu_D$ and $\Delta\nu_L$, in the following:

$$\Delta \nu_{Voigt} = \frac{\Delta \nu_L}{2} + \left[\left(\frac{\Delta \nu_L}{2} \right)^2 + \Delta \nu_D{}^2 \right]^{\frac{1}{2}} \qquad [16]$$

At later delay times such as 5 μs, the plasma temperatures typically ranged from 8000-10000 K[84] which yields Doppler widths ranging from 0.0458-0.0512 Å for the carbon 247.8561 transition. The total experimental line widths, for this same carbon neutral line at these delay times, ranged from 0.6 – 1 Å. The typical trend was seen with the 193.0905 nm transition. This indicates that the line was broadened by Lorentzian processes. This means that the total line width was indicative of the Lorentzian width. Additionally the Lorentz width of these 2 carbon lines was primarily due to Stark broadening.[69] This means that the line width change indicated the a change the in number density of electrons and the plasma temperature. The line widths as a function of delay time are shown, for both the 193.0905 and 247.8561 nm transitions at three different carbon dioxide partial pressures of 5, 10 and 100 torr, in Figures 3-31 and 3-32.

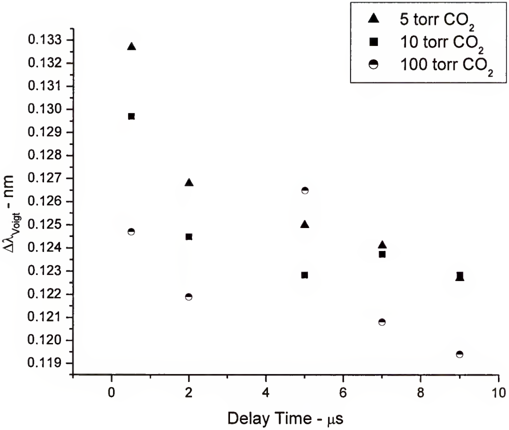

Figure 3-31: Experimental Voigt line widths for the 247.8561 nm as a function of delay time for 3 carbon dioxide partial pressures of 5, 10 and 100 torr for 148 mJ/pulse laser energy.

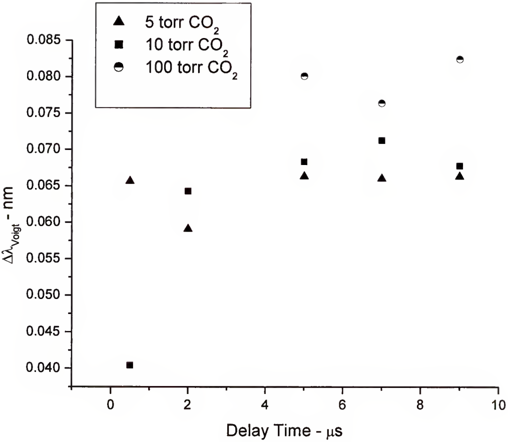

Figure 3-32: Experimental Voigt line widths for the 193.0905 nm as a function of delay time for 3 carbon dioxide partial pressures of 5, 10 and 100 torr for a laser pulse energy of 148 mJ/pulse.

The line widths for C 193.0905nm decreased as a function of time for the 247.8561 nm transition; however, the line widths for the 193.0905 nm transition did not exhibit this same decrease due to the different relationship between the electron number density and the Stark broadening. The relationship between these two parameters, termed the broadening parameter, was different for every transition.[75] The 0.5 and 2 μs points were left out because these spectra exhibited self reversal, which decreased the maximum intensity of the spectral line and therefore did not allow an accurate measurement of the spectral line width. The decrease of the line width for the 193.0905 nm transition, because the line was Stark broadened and Stark line widths are a function of plasma temperature and electron number density, confirmed that the electron density and the temperature in the plasma were decreasing at later times in the plasma.

A sample of spectra of the C 193.0905 line for various partial pressures of carbon dioxide at a delay time of 0.5 μs is shown in Figure 3-33. Self reversal occurred, which indicated either there were parts of the plasma that were much cooler than the hot center region or that extreme self absorption, was occurring. This confirms that while other data showed that the overall temperature in the temperature may not be decreasing significantly, the presence of temperature gradients in the plasma was more prevalent as the partial pressure of carbon dioxide is increased.

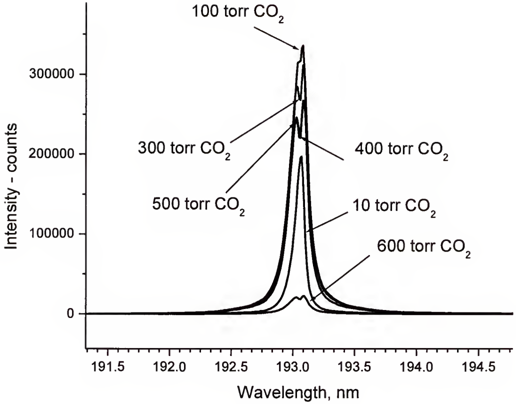

Figure 3-33: Spectra for the 193.0905 transition exhibiting self absorption for instrumental conditions of a laser pulse energy of 148 mJ/pulse and a delay time of 0.5 μs and gate width of 0.1 μs on the gated iCCD.

Another cause of the decline in emission intensity is that as the concentration of carbon dioxide increased a cooler layer of non-excited atoms was created. This cooler layer would absorb the carbon line emission causing the emission intensity to decrease as the concentration increased. A correction of this effect, otherwise termed the post-filter effect, was only available for optically thin transitions. Additionally, the plasma radiation of the plasma could also be absorbed and emitted as fluorescence. This, however, could not be proven to exist in the plasma because detection of the fluorescence required the ability to spatially separate the plasma emission from the fluorescence. This could not be achieved for the small plasmas created in LIBS.

The final reason for the decline in emission intensity was the possible incomplete dissociation of CO_2. The carbon dioxide bond is strong, 799 kcal/mole,[84] making it difficult for even the plasma to completely dissociate the carbon dioxide. However, this would not cause curvature as long as the carbon dioxide was dissociated to the same extent at all points in the calibration curves. To examine if carbon dioxide was dissociated to the same extent throughout the calibration plot, a calibration plot for the oxygen was generated. This plot would be linear if the fraction of dissociated CO_2 is constant. The oxygen emission signal was measured using the peak area from the optically thin oxygen triplet (O (I) 777.19 nm, 777.42 nm, 777.54 nm). These plots are shown in Figures 3-34 through 3-38.

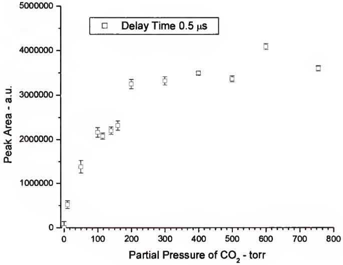

Figure 3-34: Calibration plot for oxygen of peak area as a function of partial pressure of CO2 for the following instrumental conditions: a laser pulse energy of 148 mJ/pulse and a delay time of 0.5 μs, and gate width of 0.1μs on the gated iCCD.

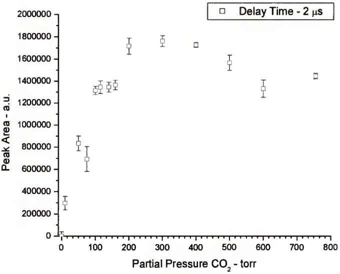

Figure 3-35: Calibration plot for oxygen of peak area as a function of partial pressure of CO2 for the following instrumental conditions: a laser pulse energy of 148 mJ/pulse and a delay time of 2 μs, and gate width of 0.1μs on the gated iCCD.

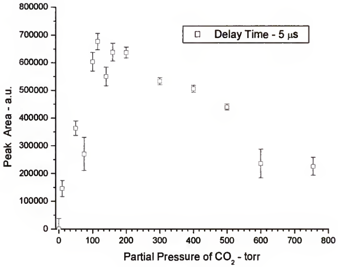

Figure 3-36: Calibration plot for oxygen of peak area as a function of partial pressure of CO2 for the following instrumental conditions: a laser pulse energy of 148 mJ/pulse and a delay time of 5 μs, and gate width of 0.1μs on the gated iCCD.

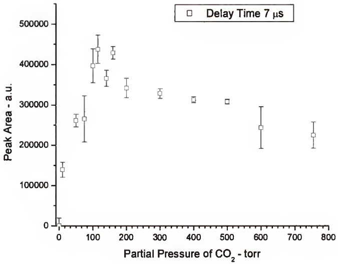

Figure 3-37: Calibration plot for oxygen of peak area as a function of partial pressure of CO2 for the following instrumental conditions: a laser pulse energy of 148 mJ/pulse and a delay time of 7 μs, and gate width of 0.1μs on the gated iCCD.

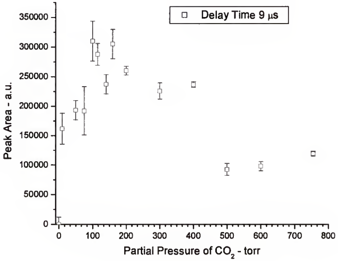

Figure 3-38: Calibration plot for oxygen of peak area as a function of partial pressure of CO2 for the following instrumental conditions: a laser pulse energy of 148 mJ/pulse and a delay time of 9 μs, and gate width of 0.1μs on the gated iCCD.

It is apparent from the curvatures in these plots, that indeed the carbon dioxide was not only dissociated incompletely but the fraction dissociated depended on the amount of CO_2 added. The same trend of increased curvature at the longer delay times was observed indicating that plasma conditions played a role in the fraction of dissociated CO_2.

To further confirm the above hypothesis, the wings of the Lorentzian profile of these lines were used to determine the number density of carbon ground state atoms. The first step was to find the frequency dependent absorption coefficient, $k(\nu)$, from the emission intensity. The emission spectra were first corrected by subtracting the dark signal from the spectra. The spectra were then examined to find the point at which the emission reached the blackbody limit, $B^b_{\lambda m}$. The emission signal, I_λ, was then normalized to this blackbody value, the plasma length, l, which was assumed to be 0.0526 cm based on previous determinations of plasma sizes at this laser power,[51] and the frequency dependent absorption coefficient was found using the following relationship:[85]

$$\frac{I_\lambda}{B^b_{\lambda m}} = \left(1 - e^{-k(\lambda)l}\right) \qquad [17]$$

$$k(\lambda)\,l = \ln \frac{B^b_{\lambda m}}{B^b_{\lambda m} - I_\lambda} \qquad [18]$$

Because the line profiles were primarily Lorentzian, the total line width, $\Delta\nu_{total}$, was related to the Lorentzian line profile by the equation:

$$P_L(\nu - \nu_0) = \frac{1}{2\pi} \frac{\Delta\nu_{total}}{(\nu - \nu_0)^2 + \left(\frac{\Delta\nu_{total}}{2}\right)^2} \qquad [19]$$

and for detuning frequencies , $(\nu-\nu_0)$, greater than the total line width the Lorentzian profile, P_L, is approximately equal to $(\nu-\nu_0)^{-2}$. This simplification allowed the following relationship to be used at the wings of the line profile, which related the frequency dependent coefficient to the number density of the ground state carbon atoms:[69]

$$k(\lambda) = \frac{e^2\ \lambda^2 \Delta\lambda_D N_0}{Z(T)} \times \frac{g_i f\ e^{-\frac{E_i}{kT}}}{(\lambda - \lambda_0)} \times \frac{\Delta\lambda_L}{\Delta\lambda_D} \qquad [20]$$

here the Doppler broadening, $\Delta\lambda_D$ cancelled out and the equation was rewritten as:

$$N_0 = \frac{k(\lambda)(\lambda - \lambda_0)^2 mc^2 Z(T)}{\lambda^2\, e^2 g_i\ f\ e^{-\frac{E_i}{kT}} \Delta\lambda_L} \qquad [21]$$

where m_e is the mass of an electron in kg, c is the speed of light in m/s, $Z(T)$ is the partition function, e is the elementary charge in C, λ is the central wavelength in m, $(\lambda\text{-}\lambda_0)$ is the detuning from the line center in m, g_i and E_i are the degeneracy and energy in J of the ground state, k is Boltzmann's constant in $J^{-1}K^{-1}$, and T is plasma temperature. The plots of number density versus detuning from the line center for the 193.0905 nm and 247. 8561 nm transitions are shown in Figures 3-39 and 3-40.

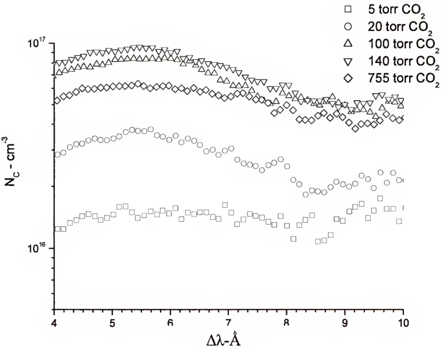

Figure 3-39: The number density of carbon atoms as found using the wings of the Lorentzian line profiles for the 193.0905 nm C(I) transition.

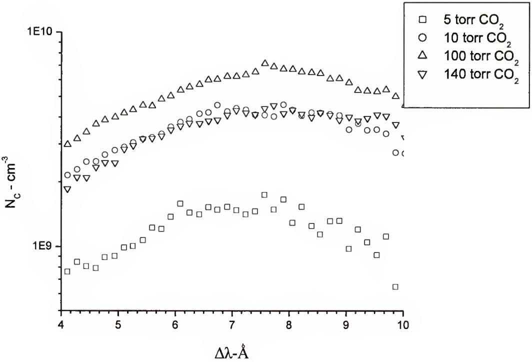

Figure 3-40: The number density of carbon atoms as found using the wings of the Lorentzian line profiles for the 247.8561 nm C(I) transition.

From the Lorentzian wings, it was apparent that the number density of carbon atoms reached a plateau and then actually decreased as the partial pressure of carbon dioxide is increased. Therefore, above 100 torr of carbon dioxide that the concentration of carbon atoms was no longer increasing, and so the increase in self reversal at pressures beyond that is indicative of severe temperature gradients and the fraction of carbon dioxide dissociated decreased as more carbon dioxide is added. The number of ground state atoms found using the wings of the 247.8561 transition was lower than expected due to the need to extrapolate the blackbody function from the value at 193.0905 to 247.8561 nm. The 247.8561 transition was not as self absorbed as the 193.0905 transition so there was never enough carbon atoms present in the plasma for the transition to reach its blackbody limit. Detector response was also different at the two wavelengths so extrapolation of the blackbody function to the 247.8561 nm transition for determination of the absorption coefficient was not accurate.

The line widths at a 5 μs delay time can also be used to determine if local thermodynamic equilibrium was established at that time in the plasma evolution. This was done by using what is termed the "broadening parameter".[69] It is defined as the ratio of the Lorentzian line width to the electron density in the plasma, and these "broadening parameters" have previously been determined for these two C(I) lines in an arc plasma. The number densities found using the experimental line widths, which are again practically equal to the Lorentzian widths under these experimental conditions, are shown in Figures 3-41 and 3-42.

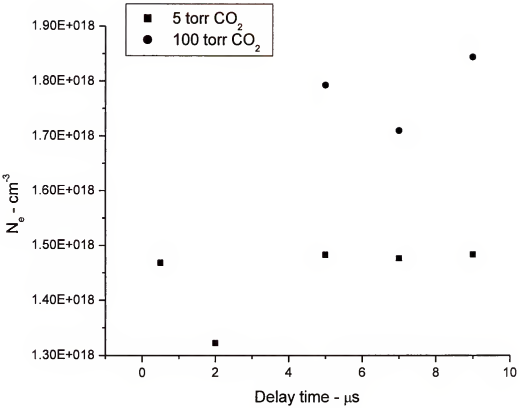

Figure 3-41: Number density of electrons, as found from the 193.0905 nm line width, for two partial pressures of carbon dioxide.

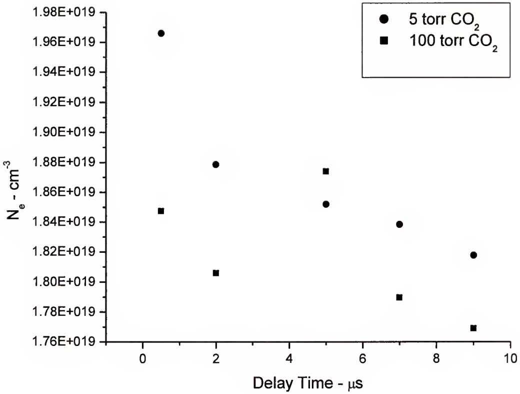

Figure 3-42: Number density of electrons, as found from the 247.8561 nm line width, for two partial pressures of carbon dioxide.

The electron number density was found to be between 1.32×10^{18} and 1.97×10^{19} using the experimental line widths from the two transitions. An electron density greater than 10^{16} indicated that indeed local thermodynamic equilibrium was established. Therefore the only probable cause for curvature of the calibration plots was the fraction of CO_2 dissociated, which changed due to changing plasma conditions.

Fitting the log-log plots of these calibration curves was attempted; however, this fitting was not successful because an optically thick region was not observed.

Conclusions and Future Work:

The cause of the decrease of the calibration plots of carbon in CO_2, with an increase in partial pressure of CO_2, was the changing plasma conditions which altered the fraction of dissociated CO_2. The temperature change along the curve was shown by the plasma continuum measurements that indicated the plasma excitation temperature for argon decayed slower than the plasma excitation temperature for carbon dioxide. An indication of the increased temperature gradients along the curve was the increased appearance of self-reversal while the number density of carbon atoms plateaued. This also indicated that the sizable temperature gradients affected the dissociation of the carbon dioxide. The calibration curves did not result in a non-linear region due only to self absorption, hence fitting log-log plots of these calibration curves to theoretical curves of growth was meaningless.

The curve of growth method could not be applied to CO_2/Ar mixture because of problems with incomplete dissociation, however, this could be overcome by using a different gas such as methane which has a much smaller bond dissociation energy of 411 kJ/mole.[84] A alternative which would guarantee a experimentally visible optically thick region, would be to use a vacuum ultraviolet (VUV) spectrometer and a setup with an evacuated path length for the plasma emission to travel so that resonance transitions, shown in Table 3-4, could be used to generate curves of growth.

Table 3-4: Resonance transitions for gases.[79]

Gas	Resonance Transitions, nm
Oxygen	60.8397, 62.9732, 78.7710, 130.2168
Nitrogen	76.5147, 98.9799, 123.8821, 124.2804
Carbon	154.8187, 155.0772
Argon	72.3361, 91.9781, 104.8220, 106.660
Neon	46.0728

If calibration plots were constructed with resonance transitions then only small amounts of analyte gas would be necessary to obtain the optically thick region. This would avoid problems associated with changing the plasma composition and result in calibration curves being described with one damping parameter. In addition, with VUV instrumentation, a nitrogen plasma could be characterized and this would be very close to characterizing an air plasma because 80% of air is nitrogen gas. Single particles could then be introduced into the plasma to determine whether plasma parameters such as number density of electrons and plasma temperature do in fact change with respect to a pure gas plasma. Further characterization of gas plasmas would give insight into the use of LIBS as a tool in the quantitative analysis of gases and this work showed that the dynamic range of LIBS even for non self absorbed transitions may only go up to 10 percent or less during the analysis of gases.

CHAPTER 4

LASER INDUCED BREAKDOWN SPECTROSCOPY AS A DETECTOR FOR SPORES

Background

Recent world events have drawn attention to the need for a real time detector of bioaerosols, specifically anthrax spores. The possibility of such spores being released into air vents or by crop planes, has also heightened the need for sensitive spore detection technologies. Using fluorescence spectrometry the presence of biological particles have been detected;[86,87] however, the fluorescent species, the amino acids (tryptophan, tyrosine,and phenylalanine), the reduced nicotinamide adenine nucleotides (NADHs), and the flavin compounds , do not vary significantly from one bioaerosol to another, so it is difficult to differentiate between pollen aerosols and bacteria aerosols. Pinnick and coworkers obtained fluorescence spectra that were significantly different for *Escherichia Coli* and *bovine serum albumin* bioaerosols, but, they are still investigating ways to further differentiate between other types of these aerosols.[88] Combining fluorescence with elastic scatter, to obtain the size and shape of the particles, resulted in improved detection of biological particles.[89]

Another optical detection method that has recently been proposed for detection of bioaerosols is Raman spectroscopy. Single particle analysis was performed on pollen, trapped by an electrodynamic balance. With a high powered diode laser at 785 nm, Kay, *et al*[90] were able to overcome the strong fluorescence background obtained with a 514 nm diode, which allowed for differentiation of different pollens by their Raman spectra.

However, the necessary trap voltages varied from particle to particle and the integration times were up to 1 minute, making real time analysis of ambient bioaerosols difficult.

Another important area of instrumentation that is crucial to detection of bioaerosols is mass spectrometry. The Chemical Biological Mass Spectrometer, from Bruker Daltonics, is a commercially available ion trap mass spectrometer, which is being used in the field for military applications.[91] Research is still being done to further improve the ease of use of the instrument and other important parameters such as power, site and maintenance requirements.[92] Another promising detection method involves the use of aerodynamic scattering in combination with positive and negative ion time-of-flight mass spectrometry. Gard and coworkers were able to distinguish between spores and typical background contaminants such as fungal spores and growth media using this instrumentation.[93]

Matrix assisted laser desorption ionization time of flight mass spectrometry (MALDI TOFMS) has recently shown potential for differentiation of bacteria species.[94] This success leads to an interest in introducing the MALDI matrix on-line. Mass spectra of *Bacillus subtillus var nigar* were obtained for mass to charge ratios below 1000 using an evaporation/condensation flow cell to introduce picolinic or sinapinic acid spiked with trifluoroacetic acid and a time of flight mass spectrometer for analysis. Identification was not possible because many of the secondary metabolites used to identify bacteria were typically found from 500-5000 Daltons, which was beyond the range of their mass spectrometer.[95] These metabolites have been found to change with growing conditions; however, success has been shown using different solvent extraction systems that produce protein fingerprints which are used for identification of spores down to the strain level.[96]

Pyrolysis gas chromatography ion-mobility mass spectrometry is now being used for real time detection of laboratory-generated bioaerosols. Here, an aerosol concentrator is combined with fast pyrolysis and gas chromatograph with an ion-mobility mass spectrometer. This technique used fatty acids for species identification.[97] The current drawbacks of mass spectrometry detection was that instrumentation was relatively large, expensive and would require frequent maintenance if reagents were necessary for analysis.

Laser Induced Breakdown Spectroscopy (LIBS), also has capability to detect biological aerosols, specifically spores. LIBS spectra of spores are spectrally rich due to trace amounts of metals present. The divalent cations of Ca, Mg, and Mn serve to chelate dipicolinic acid present in the spore core. These cations along with other cations, such as Fe, Na, and K, are bound to small molecules such as 3-phosphoglyceric acid or glutamic acid.[98]

Recent work has been performed on dry powder spores of *Bacillus subtilis var nigar* which were aerosolized using a loud speaker and transported to a chamber for LIBS analysis using 5-20 L/min air.[53] Calcium, magnesium, and sodium emission lines were obtained for various spore particles using an intensified charge coupled device (iCCD) as the detector. The number density and size of these particles were not characterized and the flow rate of air was varied to change the hit rate of the spores. LIBS spectra of solid powders of *Bacillus subtilis var nigar*, growth media, fungal spores, and pollen, taken with a more cost effective and portable broadband detector with a non-intensified CCD, were used to construct Principal Component Analysis (PCA) plots. Classification of different types of biological samples based on these plots is unlikely due to overlap between some of the spectra from the various samples. They also found that growing the spores in different media increased the within class variation and thus may hinder classification.

The goal of this work was to analyze single spores of *B. licheniformis* while characterizing the number density and size distribution of the aerosol. Spectra found via bulk analysis of spores along with PCA of the spectra will be presented to discuss the possibility of differentiation between spore species and to further examine limitations of the technique.

Theoretical Considerations

The first consideration in performing single spore analysis was to determine if the LIBS system was capable of this analysis. The expected intensity of the emission signal, I, in counts can be derived from the product of the radiance Φ_E in photons/s, the sensitivity of the detector η_0 in counts/photon, and the lifetime of the plasma t in seconds.[77]

$$I = \Phi_E \, \eta_0 \, t \qquad [1]$$

The radiance Φ_E, can be found from the transition probability A_{ji} s^{-1}, the excitation fraction, E_F, the number of total analyte atoms n_{oa}, the fraction of analyte species in that are atoms or ions α_{ion} or α_{atom}, and the fraction of plasma emission volume collected f_V.

$$\Phi_E = A_{ji} \; E_F \; n_{0a} \; \alpha \; f_V \qquad [2]$$

The fraction of analyte species that are atoms or ions, α_{atom}or α_{ion}, was found using the neutral and ionic partition functions, the plasma temperature, and the ionization energy in the Saha equation. The excitation fraction can be determined by the following equation:

$$E_F = \frac{g_j}{Z(T)} e^{-\frac{E_j}{kT}} \qquad [3]$$

here g_j is the degeneracy of the upper level, E_j and energy levels of the upper and state in J^{-1}, k is Boltzmann's constant in $J^{-1}K^{-1}$, and T is plasma temperature. It was previously determined by Carranza and others[49] that the delay time on the iCCD that gave the optimum peak to base signal, regardless of laser power, yielded a temperature of ~11,500 K. It is desirable to work at a plasma temperature which would yield the largest peak to base, hence a plasma temperature of 11,500 K was chosen for these calculations. Although the temperature measurements were performed on iron oxide aerosols using the optimal delay time for the 247.85 nm carbon transition peak to base, this same temperature should be a good estimation to obtain the maximal emission signal in this work.

When using a low powered laser to produce a LIBS plasma, a plasma may not be created for every laser shot. This is reflected in the efficiency of plasma formation, ε_{plasma}. An additional consideration is that the plasma may not completely vaporize the spore particle and this is reflected in the efficiency of vaporization, ε_{vap}. These factors must be taken into account when the number of atoms probed n_{prob}, which will take the place of n_{0a}, is calculated. These factors cannot be determined and have a large effect on the calculations. The number of atoms probed can be found from the number that would be ablated if the spark formed and efficiently vaporized and ablated the sample n_{prob}, using this equation.

$$n_{prob} = n_{0a}\, \varepsilon_{ablation}\, \varepsilon_{vap} \qquad [4]$$

The number of analyte atoms, n_{0a}, for these calculations was estimated by assuming a particle diameter of 1 μm and a density of 1.00 g/ml. The mass of a single spore was therefore 0.5 pg. The concentrations of Mg and Ca along with other cations were previously ascertained for a variety of spore species. Concentrations of these cations were determined by digesting the spores in hydrochloric acid and analyzing the digested material by atomic absorption spectroscopy. The range of Mg and Ca concentrations found in this analysis was 0.5-0.7 % and 0.21-0.5% respectively,[98] corresponding to concentrations of 9.08×10^7 and 3.93×10^7 atoms of Mg and Ca per spore particle, respectively.

The fraction of volume of collected plasma emission is found using the throughput of the system and the area of the plasma A_e, in mm^2, in the following equation:[77]

$$f_V = \frac{(w_s h_s \Omega_e T_0)}{4\pi A_e} \qquad [5]$$

where w_S and h_S are the width and the height of the slit in mm, and Ω_e and T_0 are the solid angle of collection and transmission of the system as determined by the optics and the spectrometer. Values for all discussed parameters are shown in Table 4-1.

Table 4-1: Numerical values for parameters utilized in single spore calculations.

Parameter	Value Mg(II) 279.55 nm	Value Ca (II) 393.366 nm
A_{ji}, *s*$^{-1}$ [99]	2.60×10^{8}	1.47×10^{8}
g_j, *dimens.* [99]	4	4
Z(T), dimens.	2.072	4.084
Energy of upper level, cm^{-1} [99]	35760.9	25414.4
Plasma temperature, K	11,500	11,500
ε_{plasma}, *dimens.*	1	1
ε_{vap}, *dimens.*	1	1
$n_0 = n_{probed}$	4.34×10^{7}	3.93×10^{7}
$\alpha_{neutral\ or\ ion}$	0.1763	0.3309
Slit width, mm	0.030	.0030
Slit height, mm	44	44
Transmission, dimens.	0.365	0.28
A_e, *mm*^{2}	0.0087	0.0087
Ω_e, *sr*	0.0186	0.0186
f_V, *dimens.*	8.197×10^{-2}	6.288×10^{-2}
Φ_E, *photons/s*	7.43×10^{12}	5.15×10^{15}
t, s	10^{-5}	10^{-5}
η_0, *counts/photon*	0.0241	0.1410
Emission signal, counts	2.18×10^{12}	7.2×10^{10}

The resulting emission signal, I_v, from these calculations demonstrates that a single spore may be detected but the signal seems to be much larger than expected. The sources of error in these calculations include: inaccurate detector calibration, single spore mass estimation, and the assumed values for the fraction of vaporization and ablation. The largest source is the estimation of the vaporization fraction because the degree to which the plasma is able to vaporize the particle varies from plasma to plasma and it cannot be determined for particles of unknown composition.

For the detection of aerosols, it is important to consider that aerosol systems are dynamic and hence the signal is transient. If all spectra taken over time are averaged, then the probability of observing a signal from a single particle in air is low. A conditional analysis algorithm was recently developed by Hahn and coworkers[40] which allowed particle spectra to be distinguished from spectra of air, vastly improving the sensitivity of LIBS analysis of aerosols. If a single spore can be detected, as indicated by the previous calculation, then a spore sampling rate, F, can be found using the volume of the plasma V_{Plasma} in cm^3, the frequency of the laser f_{laser} in Hz, and the number density of spore particles probed N in cm^{-3}.

$$F = N\ f_{laser}\ V_{plasma} \qquad [6]$$

The spore sampling rate allows for the minimum sampling time to be estimated if the number density of the spores is known. The parameters used in these calculations are shown in Table 4-2.

Table 4-2: Parameters used for spore sampling rate calculation.

Parameter	Value Mg(II) 279.55 nm	Value Ca (II) 393.366 nm
f_{laser}, Hz	5	5
V_{plasma}, mm^3 [51]	1.17	1.17

Experimental

Spore Samples

Stocks of *B. licheniformis* ATCC 14580, *B. pumilus* ATCC 7061, *B. gibsoni* ATCC , *B. subtilis* ATC 6057, and *B. megaterium* ATC 14581 were procured from the American Type Culture Collection. Spores were prepared by Danielle Dickinson at the University of Florida according to protocol described elsewhere.[96] Microcosms that attained greater than 99% sporulation were further purified to remove vegetative cells or cell debris by established protocols. The concentration of the spores in the stock solution was adjusted to give 10^8-10^9 spores/ml based on the optical density measurement at 600 nm. To test the effect of varying growth conditions Standard Nutrient Sporulation Medium (NSM) was modified by eliminating the addition of excess Ca^{2+} and increasing the amount of excess Mg^{2+} added to the solution.

LIBS Setup

Single Spore Detection

The experimental system used for the detection of single aerosol spores has been described in detail by Hahn[42] but will be described here briefly. A pulsed Nd:YAG laser (1064 nm, 10 ns pulse width, 400 mJ/pulse, Continuum Laser, Santa Clara, California) was expanded via a telescope, directed through a pierced mirror, and focused with a planoconvex lens (75 mm focal length, 50 mm diameter, UV grade). The plasma emission was collimated and collected with the same lens and directed with the pierced mirror to an additional planoconvex lens (75 mm focal length, 50 mm diameter, UV grade) which focused the plasma emission onto a fiber optic bundle. The fiber optic bundle was coupled to a 0.25 m spectrometer (SpectroPro-250i, Acton Research Corporation, Acton, Massachusetts) with 1200 and 2400 g/mm gratings. The 1200 g/mm grating, with a 0.035 nm/pixel linear dispersion, was used for this analysis. The spectrometer separated the plasma emission and dispersed it onto the face of the intensified charge coupled device (iCCD) which was powered and controlled by a pulse generator (ST-138S, PG200, ITE/CCD-576, Princeton Instruments, Trenton, New Jersey). A schematic of this setup is shown in Figure 4-1.

A well characterized aerosol generator system comprised of a pneumatic type medical nebulizer (Hudson, model #1724) and a mixing and drying section generated the aerosolized spores.[82] The nebulizing and co-flow gas flow of compressed air was fixed at 5 L/min and 42 L/min. The spores were analyzed for Ca, Mg, K, and Na. Because each spectral window is only 30 nm, the spectrum of each element was taken at separate times. Optimal delay times and gate widths for typical transitions during the analysis of pure aerosols of comprised of these elements have previously been found.[48] These same conditions were used in these experiments and are listed with their corresponding transitions in Table 4-2. The conditional analysis was set to yield 1-2 false hits per 1000 spectra.

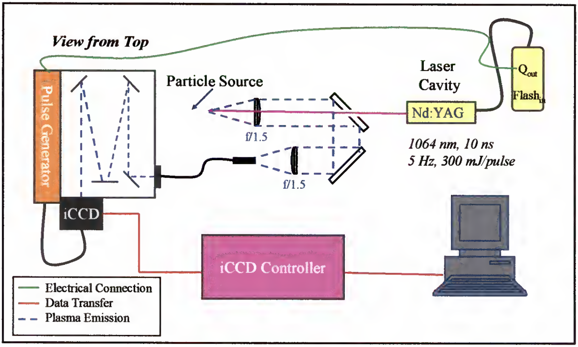

Figure 4-1: Schematic of instrument setup.

Table 4-2: The transitions, delay times, and gate widths

Element	*Spectral Lines, nm*	*Gate Delay, µs*	*Gate Width, µs*
Mg	279.079, 285.213	40	40
Ca	393.366, 396.847	40	40
K	404.414, 404.721	30	30
Na	588.995	40	40

Determination of the concentration the *B. licheniformis* stock solution was necessary to insure that during aerosol generation only 1 spore would be present per plasma. Plate counting of the *B. licheniformis* did not yield consistent data and thus the exact concentrations of the dilutions were back calculated from count distributions provided by the laser particle counter (Model 1001, Particle Measuring Systems, Worcestershire, England), which was able to size and count particles from 0.1-2 μm in diameter. These distributions are shown in Figure 4-2 and 4-3. The spores were assumed to be 0.5 -1 μm in diameter and the large concentration of smaller particles in both solutions was due to broken down vegetative cells or spores. These size distributions reflect the relative number of particles in each size range; the raw counts not the percent in values, are used for number density calculations.

The concentrations of the particles, specifically spores, in particles/mL were calculated using the sampling rate of the particle counter, 280 mL/min, and the instrument sampling time, 5 minutes. The resulting number densities of 3 spores/cm^3 and slightly greater than 4 spores/cm^3 were then used to back calculate the concentration of the spores in the solution using the following equation:

$$number\ density\ of\ spores = \frac{spore\ solution\ concentration \times nebulization\ rate}{co - flow + nebulizing\ flow} \qquad [7]$$

the coflow and nebulizing, flow rate as stated above, were 42 and 5 L/min and the nebulization rate was 0.09 mL/min. The concentrations of the two *Bacillus licheniformis* spore solutions were calculated as 1.567×10^6 and 2.274×10^6 spores/ml. This did not correspond to dilutions performed in the laboratory because spores stick to plastic which was what comprised both the nebulizer and dilution vials. These concentrations still met the requirement of single particles sampling, which is less than 4000 spore particles/cm^3, with spore number densities of 3 and slightly greater than 4 spore particles/cm^3. The only effect would be lower spore sampling frequencies.

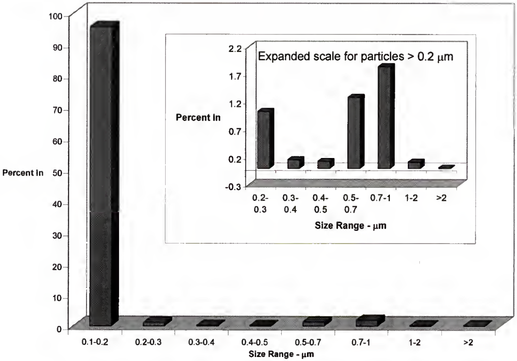

Figure 4-2: Particle size distribution for the 3 spores/cm^3 aerosol.

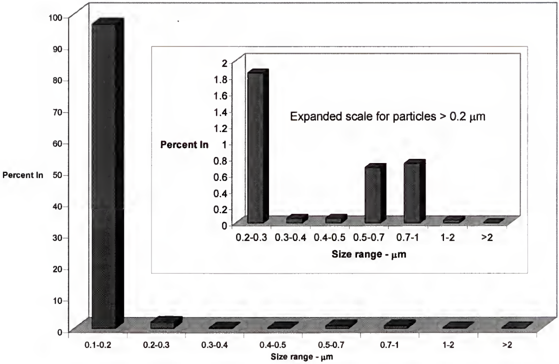

Figure 4-3: Particle size distribution for the ~4 spores/cm^3 aerosol.

Eight hundred spectra were taken at each spectral window for the aerosols generated from two *Bacillus licheniformis* spore solutions. Other spore species were not measured due to the questionable safety of aerosolizing these species.

Bulk Analysis

Bulk analysis of spores was performed using a pulsed Nd:YAG laser(1064 nm, 10 ns pulse width, 50 mJ/pulse, Big Sky Laser, Big Sky, Montana) which was focused through a lens (75 mm focal length, 25 mm diameter) to form a plasma on the spore sample. The sample was on an x-y-z stage so it could be moved to obtain a fresh spot for every ablation event. The resulting plasma emission was collected with a collimating lens (20 mm focal length, 10 mm diameter) and focused onto a fiberoptic bundle with 7, 600 µm fibers, each went to a different grating or order to cover a certain spectral window typically 100-150 nm wide. Each grating possessed a non-intensified charge coupled device (CCD) to detect plasma emission. This system was compact and cost effective providing a spectral window from 200-980 nm (HR2000 Broadband Spectrometer, Ocean Optics Inc., Dunedin, Florida). Spectrometer acquisition could be delayed for time resolved measurements. This was achieved by changing the timing between the flashlamp and the Q switch. A schematic of the setup is shown in Figure 4-4. A delay time of 1.5 µs was chosen because it yielded the highest signal to background in analysis of surrogates comprised of magnesium hydroxide, $Mg(OH)_2$, and calcium oxide, CaO, and graphite.

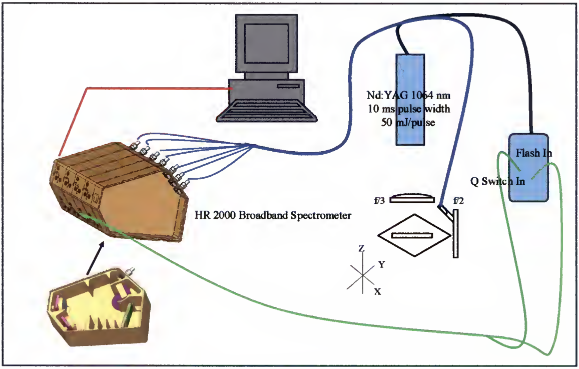

Figure 4-4: Schematic of the LIBS setup used for bulk analysis

The spores were deposited onto double sided tape to ellicit spectral features of the various Bacillus species. One hundred µL of the stock spore solution, 10^8-10^9 spores/mL, was deposited onto a 1 cm square of the doubled sided tape and the sample was dessicated for 8 hours to yield dry spore samples that were ready to be used for analysis.

It is known that LIBS of bulk solutions was a problem due to splashing and that differing amounts of water in the sample altered the LIBS signal,[101,102] hence dry spores were necessary for analysis. The double sided tape was chosen because it exhibited the least amount of spectral interferences. Spectra of all evaluated potential matrices are shown in Figure 4-5.

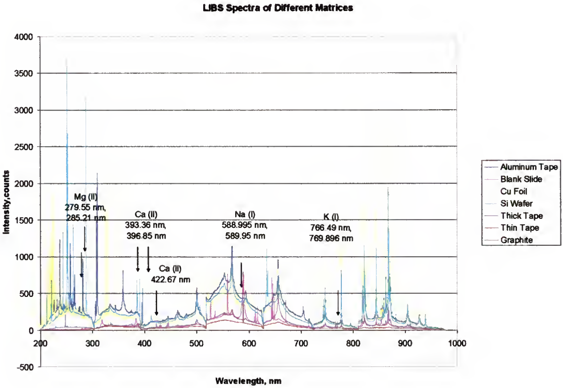

Figure 4-5: Spectra of potential matrices for spore analysis.

Results and Discussion

Single Spore Detection

The only element which could be detected via LIBS analysis of *Bacillus licheniformis* was calcium. The single spore calcium spectra for each concentration, 3 particles/cm^3 and ~ 4 particles/cm^3, are shown in Figures 4-6 and 4-7.

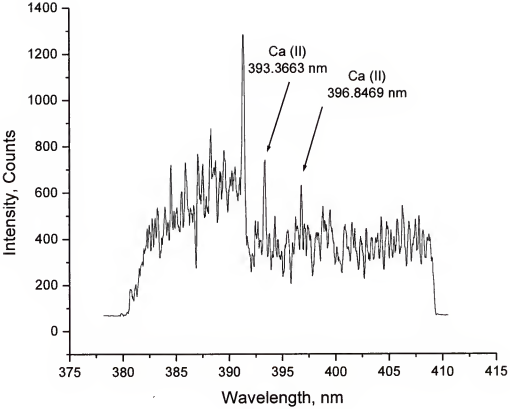

Figure 4-6: The only calcium hit for the concentration of 3 spores/cm^3. Spectrum is a single *B. licheniformis* spore.

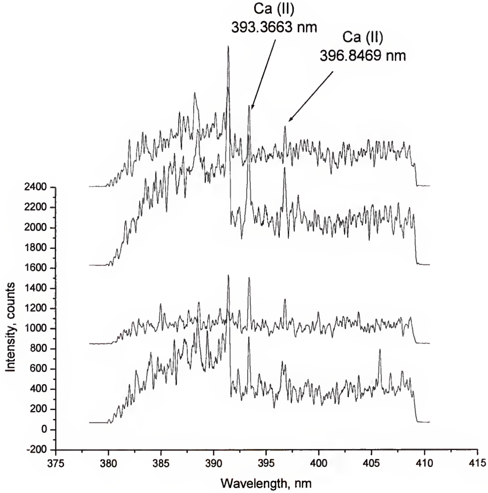

Figure 4-7: The four calcium hits for the concentration of ~4 spores/cm^3. Each spectrum is a single *B. licheniformis* spore.

It is apparent that single spore analysis may not be possible because only calcium and none of the other elements were detected. The number of hits for each number density was 1 and 4. Using equation 3, the spore number density, and the number of shots in conjunction with frequency of the laser to obtain the sampling time, a spore sampling frequency can be found. Each run took 160 s, and the first run yielded 1 hit while the second yielded 4 hits. Therefore, it took on average 160 s to sample one spore for an aerosol with a number density of 3 spores/cm^3 and it took 40 s to sample one spore for an aerosol with a number density of ~ 4 spores/cm^3. This could be due to inhomogeneity in the aerosol distribution.

In addition to not being able to observe detectable spectral lines of other elements to confirm the presence of the spores versus other inorganic particles present in ambient air, spore agglomerates or lysed spores may be mistaken for a single spore and for single spore analysis such particles contaminants. Spectral contamination was seen with the more concentrated solution. The higher concentration was favorable for aggregate formation. Spectra of both a contaminant particle and an actual single spore are shown in Figure 4-8. The calcium intensity from the contaminant particle is greater than 3 times the intensity from the spore particle.

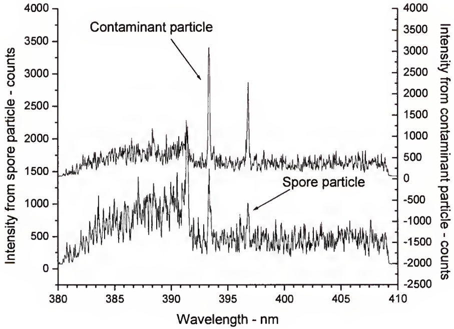

Figure 4-8: Single shot spectra of contaminant and spore particles.

This work demonstrates that because intense spectral lines were observed for contaminant particles that are most likely spore agglomerates, agglomerate analysis may be possible. There is a need for a larger spectral window and a cheaper and more portable system to distinguish between Bacillus spores and other inorganic agglomerates. The spectra from the Bacillus family also may exhibit different spectra depending on their species type. This is base purely on the principal that different species may take up different amounts of these metals during spore formation. The broadband Ocean Optics HR2000 spectrometer, measures emission spectra from these spores over a wide wavelength range allowing these spectral features to be examined.

Bulk Analysis

A typical spectrum of *Bacillus licheniformis*, with characteristic peaks labeled, is shown in Figure 4-9. Spectra of *Bacillus licheniformis*, *pumilus*, *megaterium*, *subtilus*, and *gibsoni* spores are shown in Figures 4-10. Spectra of these spores do show characteristic features, however, the averaged spectrum for *B. gibsoni* did not have spectral features in 710-810 nm spectral range due to a broken fiber.

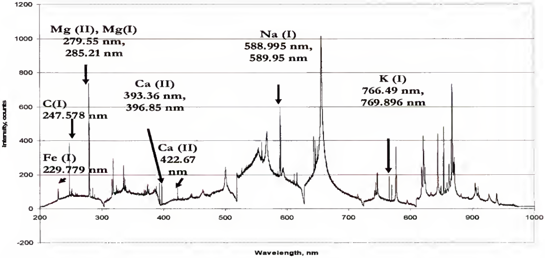

Figure 4-9: LIBS spectrum of *B. licheniformis* with characteristic peaks.

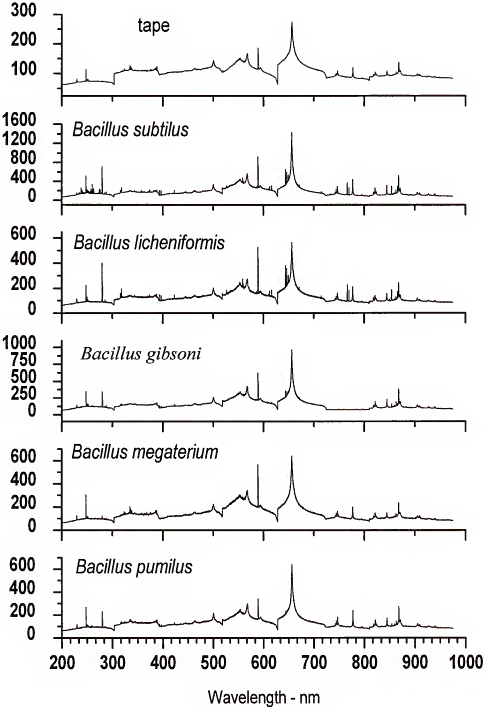

Figure 4-10: LIBS spectra for various *Bacillus* species and for the substrate double sided tape. .

The LIBS spectra of the *Bacillus subtilus* grown with and without calcium added to growth media are shown in Figure 4 -11.

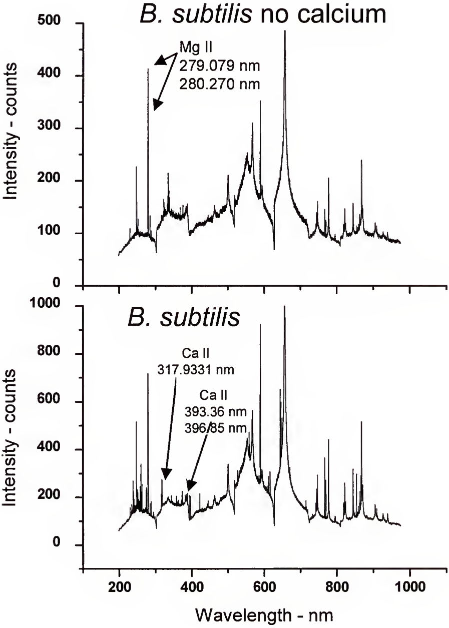

Figure 4-11: LIBS spectra of *B. subtilis* grown with calcium added to the growth media and without.

These spectra differ not only by the presence and absence of calcium lines but also by the relative intensity, the signal to background, of the magnesium. Because the spectra from the various spore species exhibit different spectral features classification was attempted using the unsupervised methods of linear correlation, rank correlation, and principal component analysis using SPSS statistical software (SPSS for Windows version 11.5, Chicago, Illinois). Due to the limit of the number of data points that the program can successfully analyze, the spectra were truncated from 14336 data points to 552. This was done by selecting regions of the spectra where intense emission lines for the various elements previously found in spores should be present. These regions along with the corresponding expected emission lines are found in Table 4-3.

Out of these classification techniques, principal component analysis was the only successful technique for discriminating between the various Bacillus species. One hundred spectra from each of the three replicates of the spores deposited on the tape and one hundred spectra from each of the two replicates of plain tape were examined. The 3 spectra with the highest signal to background from each of the replicates were used for further statistical analysis. In principal component analysis, the dimensions of the data were reduced to reflect the variance within the data. The data matrix was broken down into two simpler matrices, the scores and the loading matrix. The scores and the loadings matrix were constructed by covariance matrices of the raw truncated data. A principal component was then defined as how the original data matrix projects onto the scores matrix. The number of columns in the scores matrix, the number of principal components, was chosen by how much variance was to be included in the analysis, which was 98% for this analysis.[103] In analyzing the truncated spectra 3 principal components were utilized and a plot of how the variance of the spectra is shown in Figure 4-12.

Table 4-3: Regions of spectra used in classification will corresponding expected emission lines.

Wavelength region, nm	Element and transition type	Transition wavelength, nm[99]
229.118-230.135	Fe (I)	229.779
247.227-252.764	C (I), Fe (I)	247.8561, 247.2336, 247.9776, 249.6553, 250.1132
278.775-280.736	Fe (I)	278.8105
	Mn (I)	279.4817
	Mg (II)	279.079
	Mg (I)	280.270
287.589-288.506	Na (II)	288.115
294.398-295.112	Fe (I)	294.778
	Mn (II)	294.9205
317.13-319.1	Ca (I)	318.128
323.262-323.91	Mn (I)	323.678
392.893-397.09	Ca (II)	393.030 396.847
421.879-423.105	Fe (I)	422.7423
588.738-589.92	Na (I)	588.995 589.592
611.608-613.092	Ca (I)	612.056
615.787-617	Ca (I)	616.129
643.217-644.335	Ca (I)	643.907
645.671-646.781	Ca (I)	646.257
648.942-650.59	Ca(I)	649.378
714.555-715.192	Ca (I)	714.815
766.21-767.025	K (I)	766.491
769.496-770.476	K (I)	769.898
853.304-855.199	Ca (II)	854.209

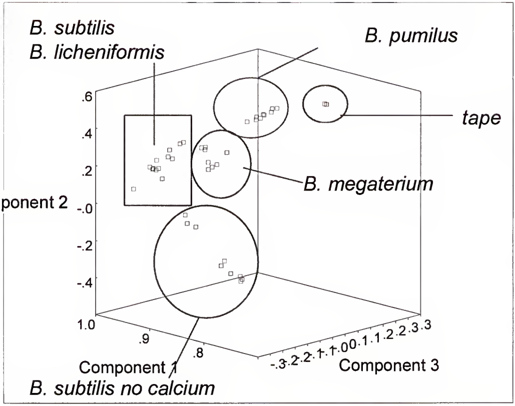

Figure 4-12: Plot of principal components for spectra of the various Bacillus species.

Separation is achieved for all but the *B. subtilis* grown under normal conditions and the *B. licheniformis*. A hindrance to the classification of the species is that the growing conditions significantly change the classification of the species. Higher concentrations of spore samples may yield more reproducible spectra further improving the clustering of the data; however, the most significant disadvantage of the broadband spectrometer system is the low sensitivity of the broadband detector. Many spectra taken exhibited little to no spectral features different from that of the substrate even though the concentration of the spores was approximately 10^7 spores/mL. This was confirmed by a comparison of the calibrated sensitivity of the two systems; the broadband detector at the

Ca wavelength of 393.3663 nm possessed a sensitivity pf 4.07×10^{-12} counts/photon versus 1.4×10^{-1} counts/photon for the iCCD.

Conclusions and Future Work

It has been shown that single spore detection with an intensified system may not be possible; however, agglomerate analysis of spores is a realistic goal for LIBS detection. If an echelle spectrometer with a prism to increase the spectral range of the intensified system were used, the identification and detection of the *Bacillus* species would be more confident based on the presence of other elements, such as Mg, K, and Na in the same agglomerate.

The broadband system may have a role in bioaerosol detection if an air sampler is used to concentrate the aerosol onto a substrate for subsequent LIBS analysis. Evaluation of the signal from background ambient aerosol and the evaluation of the necessary sampling time for detection of bioaerosol are the first steps to accessing the feasibility of LIBS detection with this low cost instrumentation.

APPENDIX A
LIST OF SYMBOLS

n_j = number density of atoms in the upper state, cm^{-3}

n_i = number density of atoms in the lower state, cm^{-3}

gj = degeneracy of the upper state, dimens.

gi = degeneracy of the lower state, dimens.

E_j = upper energy level, J

E_i = lower energy level, J

k = Boltzmann's constant, J K^{-1}

T = plasma temperature, K

A_{ji} = transition probability, s^{-1}

I_λ = spectral intensity as a function of wavelength, W m^{-2} sr^{-1}

λ_0 = wavelength of the transition, cm

n_e = number density of electrons, cm^{-3}

n_a = number density of atoms, cm^{-3}

n_{a+1} = number density of ions, cm^{-3}

m_e = mass of an electron, kg

h = Planck's constant, J s

$Z_a(T)$ = partition function of the atoms, dimens,

$Z_{a+1}(T)$ = partition function of the ions, dimens.

E_{ion} = ionization energy, J

PSR = particle sampling rate, dimens.

μ = average number of particles per spark, dimens.

x = mass concentration, μg/m^3

V_{Plasma} = volume of the plasma, cm^3

ρ = density of the particle, g/cm^3

d_{VMD} = diameter of the particle, m

m_a = mass of analyte, μg

D = equivalent spherical diameter, cm

V_S = statistical plasma volume, cm^3

F = particle sampling frequency, dimens.

N = number density of the particles, cm^{-3}

V_e = emission plasma volume, cm^3

C = actual mass concentration, μg/m^3

$\overline{m}$ = mean aerosol mass, μg

X = equivalent mass concentration found from the ensemble averaged particle spectra

A_t = total absorption, Hz

$k(v)$ = frequency dependent absorption coefficient, cm^{-1}

l = absorption path length, cm

I_v = spectral line intensity, W m^{-2} sr^{-1}

$B^b{}_{vm}$= blackbody spectral radiance at line center, W m^2 sr^{-1}Hz^{-1}

c = speed of light, m/s

v = frequency of transition, Hz

n_0 = number density of analyte atoms, cm^{-3}

$\Delta\nu_D$ = Doppler broadening, Hz

$\Delta\nu_L$ = Lorentzian broadening, Hz

a = damping parameter, dimens.

ν_0 = frequency of transition, Hz

m = mass of emitting atom, kg

w = electron impact half width, m

d/w = shift to width ratio, dimens.

α = ion broadening parameter, dimens.

$\Delta\lambda_{Stark\ shift}$ = Stark shift, m

$\Delta\lambda_{Stark\ width}$ = Stark width, m

υ = relative velocity of atoms, m/s

n_{pert} = number density of perturbing atoms, m^{-3}

C_6 = interaction potential constant, m^6/s

$\Delta\lambda_{Vander\ Shift}$ = Van der waals shift, m

$\Delta\lambda_{Vander\ width}$ = Van der waals width, m

$\sigma(\lambda)$ = optical cross section as a function of wavelength, cm^{-2}

$k(\lambda)$ = absorption coefficient as a function of wavelength, cm^{-1}

f_{ij} = oscillator strength, dimens.

$S(\lambda)$ = spectral profile function as a function of wavelength, cm^{-1}

$\Delta\lambda_{eff}$= spectral line kernel, cm

$k(\lambda_0)$ = maximum absorption coefficient, cm-1

$k(\lambda)d\lambda$ = area under spectral profile function

$\Delta\nu_{Voigt}$ = Voigt width, Hz

$B^b{}_{\lambda m}$ = blackbody radiance at line center, W m^2 $sr^{-1}nm^{-1}$

I_λ= spectral intensity as a function of wavelength, W m^{-2} sr^{-1}

Δv_{total} = total line broadening, Hz

P_L = Lorentzian line profile

$\Delta\lambda_D$ = Doppler line width, m

$\Delta\lambda_L$ = Lorentzian line width, m

Φ_E = radiance, photons/s

η_0 = sensitivity of the detector, counts/s

t = lifetime of the plasma, s

E_F = excitation fraction, dimens.

α_{atom} = fraction of analyte species that are atoms, dimens.

α_{ion} = fraction of analyte species that ions, dimens.

f_V = fraction of plasma emission collected, dimens.

ε_{plasma} = efficiency of plasma formation, dimens.

ε_{vap} = efficiency of vaporization, dimens.

n_{0a} = number of atoms, atoms

n_{prob} = number of atoms probed, atoms

w_S = width of slit, mm

h_S = height of slit, mm

A_e = area of plasma emission, mm^2

T_0 = transmission of optics, dimens.

Ω_e = solid angle of collection, sr

f_{laser} = repetition rate of laser, Hz

LIST OF REFERENCES

1. Maiman, T. H. *Nature* **1960,** *187*, 493-94.

2. Brech, F.; Cross, L. *Appl. Spectrosc.* **1962,** *16*, 59.

3. Maker, P. D.; Terhune, R. W.; Savage, C. M. *Optical third harmonic generation in various solids and liquids in Proc. 3rd Int. Conf. On Quantum Electronics* Grivet, P.;Bloembergen, N., Eds.; 1964; pp1559-1565.

4. Rusak, D. A.; Castle, B. C.; Smith, B. W.; Winefordner, J. D. *Crit. Rev. in Anal. Chem.* **1997,** *27*, 257-90.

5. Schechter, I. *Rev. in Anal. Chem.* **1997,** *16*, 173-298.

6. Radziemski, L. J.; Cremers, D. A. *Laser Induced Plasmas and Applications,* Marcel Dekker: New York, 1989.

7. Martin, M. Z.; Cheng, M. D.; Martin, R. C. *Aerosol. Sci. Technol.* **1999,** *31*, 409-21.

8. Smith, B. W.; Hahn, D. W.; Gibb, E.; Gornushkin, I. B.; Winefordner, J. D. *Kona* **2001,** *19*, 25-33.

9. Tozer, B. A. *Phys. Rev.* **1965,** *137*, 1665-&.

10. Morgan, C. G. *Reports on Progress in Phys.* **1975,** *38*, 621-&.

11. Lencioni, D. E.; Pettingill, L. C. *J. Appl. Phys.* **1977,** *48*, 1848-51.

12. Essien, M.; Radziemski, L. J.; Sneddon, J. *J. Anal. At. Spectrom.* **1988,** *3*, 985-88.

13. Hsieh, W. F.; Eickmans, J. H.; Chang, R. K. *J. Opt. Soc. Am. B* **1987,** *4*, 1816-20.

14. Pinnick, R. G.; Biswas, A.; Pendleton, J. D.; Armstrong, R. L. *Appl. Opt,* **1992,** *31*, 311-18.

15. Radziemski, L. J.; Loree, T. R.; Cremers, D. A.; Hoffman, N. M. *Anal. Chem.* **1983,** *55*, 1252-56.

16. Lochte-Holtgreven, W. *Plasma Diagnostics,* North-Holland Publishing Company: Amsterdam, 1968.

17. Boumans, P. W. *Theory of Spectrochemical Excitation,* Plenum Press: New York City, 1966.

18. Thorne, A. P. *Spectrophysics,* J.W. Arrowsmith: Bristol, England, 1988.

19. Tambay, R.; Thareja, R. K. *J. Appl. Phys.* **1991,** *70*, 2890-92.

20. Davis, J. P.; Smith, A. L.; Giranda, C.; Squicciarini, M. *Appl. Opt,* **1991,** *30*, 4358-64.

21. Davis, L. M.; Li, L. Q.; Keefer, D. R. *J. Phys. D: Appl. Phys.* **1993,** *26*, 222-30.

22. Simeonsson, J. B.; Miziolek, A. W. *Appl. Phys. B-Lasers and Optics* **1994,** *59*, 1-9.

23. Takahashi, A.; Nishijima, K. *Jap. J. Appl. Phys.* **1995,** *34*, 2471-75.

24. Minowa, T.; Kawata, T.; Katsuragawa, H.; Uematsu, H. K. *Appl. Opt,* **1998,** *37*, 1099-103.

25. Gamal, Y. E.; Shafik, M. S.; Daoud, J. M. *J. Phys. D: Appl. Phys.* **1999,** *32*, 423-29.

26. Yalcin, S.; Crosley, D. R.; Smith, G. P.; Faris, G. W. *Appl. Phys. B* **1999,** *68*, 121-30.

27. Hanafi, M.; Omar, M.; Gamal, Y. E *Radiat. Phys. Chem.* **2000,** *57*, 11-20.

28. Martin, F.; Mawassi, R.; Vidal, F.; Gallimberti, I.; Comtois, D.; Pepin, H.; Kieffer, J. C.; Mercure, H. P. *Appl. Spectrosc.* **2002,** *56*, 1444-52.

29. Carranza, J. E.; Hahn, D. W. *Anal. Chem.* **2002,** *74*, 5450-54.

30. Cremers, D. A.; Radziemski, L. J. *Anal. Chem.* **1983,** *55*, 1252-56.

31. Williamson, C. K.; Daniel, R. G.; McNesby, K. L.; Miziolek, A. W. *Anal. Chem.* **1998,** *70*, 1186-91.

32. Lancaster, E. D.; McNesby, K. L.; Daniel, R. G.; Miziolek, A. W. *Appl. Opt.* **1999,** *38*, 1476-80.

33. Dudragne, L.; Adam, P.; Amouroux, J. *Appl. Spectrosc.* **1998,** *52*, 1321-27.

34. Lancelin, H.; Dudragne, L.; Adam, P.; Amouroux, J. *High Temp. Mater. Processes* **2000,** *4*, 109-26.

35. Singh, J. P.; Zhang, H. S.; Yueh, F. Y.; Carney, K. P. *Appl. Spectrosc.* **1996,** *50*, 764-73.

36. Arnold, S. D.; Cremers, D. A. *Am. Ind. Hyg. Assoc. J.* **1995,** *56*, 1180-86.

37. Schechter, I. *Anal. Sci. and Technol.* **1995,** *8*, 779-86.

38. Peng, L. W.; Flower, W. L.; Hencken, K. R.; Johnsen, H. A.; Renzi, R. F.; French, N. B. *Process Control Qual.* **1995,** *7*, 39-49.

39. Singh, J. P.; Yueh, F. Y.; Zhang, H. S.; Cook, R. L. *Process Control Qual.* **1997,** *10*, 247-58.

40. Hahn, D. W.; Flower, W. L.; Hencken, K. R. *Appl. Spectrosc.* **1997,** *51*, 1836-44.

41. Hahn, D. W. *Appl. Phys. Lett.* **1998,** *72*, 2960-62.

42. Hahn, D. W.; Lunden, M. M. *Aerosol. Sci. Technol.* **2000,** *33*, 30-48.

43. Nunez, M. H.; Cavalli, P.; Petrucci, G.; Omenetto, N. *Appl. Spectrosc.* **2000,** *54*, 1805-16.

44. Tran, M.; Smith, B. W.; Hahn, D. W.; Winefordner, J. D. *Appl. Spectrosc.* **2001,** *55*, 1455-61.

45. Martin, M.; Cheng, M. D. *Appl. Spectrosc.* **2000,** *54*, 1279-85.

46. Gleason, R. L.; Hahn, D. W. *Spectrochim. Acta Part B At Spectrosc..* **2001,** *56*, 419-30.

47. Fisher, B. T.; Johnsen, H. A.; Buckley, S. G.; Hahn, D. W. *Appl. Spectrosc.* **2001,** *55*, 1312-19.

48. Carranza, J. E.; Fisher, B. T.; Yoder, G. D.; Hahn, D. W. *Spectrochim. Acta Part B At Spectrosc.* **2001,** *56*, 851-64.

49. Carranza, J. E.; Hahn, D. W. *Spectrochim. Acta Part B At Spectrosc.* **2002,** *57*, 779-90.

50. Mokhbat, E. A.; Hahn, D. W. *Appl. Spectrosc.* **2002,** *56*, 984-93.

51. Carranza, J. E.; Hahn, D. W. *J. Anal. At. Spectrom.* **2002,** *17*, 1534-39.

52. Carranza, J. E.; Gibb, E.; Smith, B. W.; Hahn, D. W.; Winefordner, J. D. *Appl. Opt.* **2003,** *42*, 6016-21.

53. Hybl, J. D.; Lithgow, G. A.; Buckley, S. G. *Appl. Spectrosc.* **2003,** *57*, 1207-15.

54. Gornushkin, I. B.; Anzano, J. M.; King, L. A.; Smith, B. W.; Omenetto, N.; Winefordner, J. D. *Spectrochim. Acta Part B At Spectrosc.* **1999,** *54*, 491-503.

55. Rachford, B. L.; Snow, T. P.; Tumlinson, J.; Shull, J. M.; Roueff, E. *The Astrophysical Journal* **2001,** *555*, 839-49.

56. Parker, J. W.; Stern, S. A.; Gladstone, G. R; Shull, J. M. *The Astrophysical Journal* **1998,** *509*, L61-L64.

57. Krasnopolsky, V. A. *J. Geophys. Res.* **2003,** *108*, 1-12.

58. Ladenburg, R; Reiche, F. *Ann. Phys.* **1913,** *42*, 181.

59. Mitchell, A. C.; Zeegers, P. J. T. *Resonance Radiation and Excited Atoms,* 3rd ed.; Cambridge University Press: New York, 1971.

60. Hinnov, E. *J. Opt. Soc. Am.* **1957,** *47*, 151-55.

61. Trigt, C. V.; Hollander, Tj; Alkemade, C. T. *J. Quant. Spectrosc. Radiat. Transfer* **1965,** *5*, 813-33.

62. Jansen, B. J.; Hollander, Tj *Spectrochim. Acta Part B At Spectrosc.* **1977,** *32B*, 165-71.

63. Omenetto, N.; Winefordner, J. D.; Alkemade, C. Th. J. *Spectrochim. Acta Part B At Spectrosc.* **1977,** *30*, 335-41.

64. Alkemade, C. Th. J.; Hollander, Tj.; Snelleman, W.; Zeegers, P. J. T. *Metal Vapours in Flames,* Pergamon Press: New York, 1982.

65. Zeegers, P. J. T.; Smith, R; Winefordner, J. D. *Anal. Chem.* **1968,** *40*, 26A-47A.

66. Smith, B. W.; Rutledge, M. J.; Winefordner, J. D. *Appl. Spectrosc.* **1987,** *41*, 613.

67. Hinnov, E.; Kohn, H. *J. Opt. Soc. Am.* **1957,** *47*, 156-62.

68. Lovett, R. J.; Parsons, M. J. *Appl. Spectrosc.* **1977,** *31*, 424-34.

69. Vadla, C; Vujnovic, V. *Phys. Rev. A* **1979,** *20*, 1573-78.

70. Aragon, C; Bengoechea, J.; Aguilera, J. A. *Spectrochim. Acta Part B At Spectrosc.* **2001,** *56*, 619-28.

71. Aguilera, J. A.; Bengoechea, J.; Aragon, C *Spectrochim. Acta Part B At Spectrosc.* **2003,** *58*, 221-37.

72. Bulajic, D; Corsi, M; Cristoforetti, G.; Legnaioli, S.; Palleschi, V.; Salvetti, A.; Tognoni, E. *Spectrochim. Acta Part B At Spectrosc.* **2002,** *57*, 339-53.

73. Lazic, V.; Barbini, R.; Colao, F.; Fantoni, R.; Palucci, A., *Spectrochim. Acta Part B At Spectrosc* .**2001,** *56*, 807-20.

74. Mavrodineanu, R. *Analytical Flame Spectroscopy,* Macmillan: New York City, 1970.

75. Griem, H. *Spectral Line Broadening by Plasmas,* Academic Press: New York City, 1974.

76. Griem, H. *Plasma Spectroscopy,* 1st ed.; McGraw Hill: New York City, 1964.

77. Ingle, J. D.; Crouch, S. R. *Spectrochemical Analysis,* Prentice Hill, Inc.:Upper Saddle River, 1988.

78. Nelson, G. *Controlled Test Atmospheres: Principles and Techniques,* 5th ed.; Ann Arbor Science: Ann Arbor, Michigen, 1980.

79. Martin, W. C., Fuhr, J. R., Kelleher, D. E., Musgrove, A., Podobedova, L., Reader, J., Saloman, E. B., Sansonetti, C. J. Wiese W. L., Mohr, P. J., and Olsen, K. *NIST Atomic Spectra Database. [2.0].* **1999**. National Institute of Standards and Technology. 1999.

80. Boumans, P. W. in *Inductively Coupled Plasma*, Elving, P. J.; Winefordner, J. D.Kolthoff, I. M., Eds.; 1st ed.; John Wiley & Sons: New York, 1985; pp 555-60.

81. Armstrong, R. A.; Lucht, R. A.; Rawlins, W. T. *Appl. Opt.* **1983,** *22*, 1573-77.

82. Hahn, D. W.; Carranza, J. E.; Arsenault, G. R.; Johnsen, H. A.; Hencken, K. R. *Rev. of Sci. Instruments* **2001,** *72*, 3706-13.

83. Whiting, E. E. *J. Quant. Spectrosc. and Radiative Transfer* **1968,** *8*, 1379-84.

84. Lide, D. L. *Handbook of Chemistry,* CRC Press: Boca Raton, Florida, **1995**.

85. Thorne, A.; Litzen, U.; Johansson, S. *Spectrophysics* Springer . Berlin, Germany, 1999.

86. Nachman, P.; Chen, G.; Pinnick, R. G.; Hill, S.; Chang, R. K.; Mayo M.W. Fernandez, G. L. *Appl. Opt.* **1996,** *35*, 1069-76.

87. Hill, S.; Pinnick, R. G.; Niles, S.; Fell, N.; Yong-Le, P.; Bottiger, J.; Bronk, B. V.; Holler, S.; Chang, R. K. *Appl. Opt.* **2001,** *40*, 3005-13.

88. Pinnick, R. G.; Hill, S.; Nachman, P.; Videen, G; Chen, G.; Chang, R. K. *Aerosol. Sci. Technol.* **1998,** *28*, 95-104.

89. Kaye, P. H.; Barton, J. E.; Hirst, E.; Clark, J. M. *Appl. Opt.* **2000,** *39*, 3738-45.

90. Laucks, M. L.; Roll, G.; Schweiger, G.; Davis, E. J. *J. Aerosol Sci.* **2000,** *31*, 307-19.

91. Block II Chemical Biological Mass Spectrometer. Bruker Daltonics, www.bdal.com.. 2003.

92. Griest, W. H.; Wise, M. B.; Hart, K. J.; Lammert, S. A.; Thompson, C. V.; Vass, A. A. *Field Anal. Chem. and Technol.* **2001,** *5*, 177-84.

93. Gard, E. E., Fergenson, D., Tobias, H., and Frank, M. *Real-Time Detection of Biological Aerosols using Bio-Aerosol Mass Spec.: Proc. 50th ASMS Conf. on Mass Spec .in Montreal, Canada* ASMS Ed.; 2002; pp 50.

94. Stowers, M. A.; Wuijckhuijse, A. L.; Marijnissen, J. C.; Scarlett, B.; van Baar, B. L. M.; Kientz, Ch. E. *Rapid Comm. Mass Spec.* **2000,** *14*, 829-33.

95. Lay, J. O. *Mass Spectrom. Rev.* **2001**,20, 172-194.

96. Dickinson, D. N., La Duc, M. T., Haskins, W. E., Gornushkin, I. B., Winefordner, J. D., Powell, D. H., and Venkateswaran, K. Species Differentiation of a Diverse Suite of Bacillus Spores Using Mass Spectrometry Based Protein Profiling. *Appl. Environ. Microbiol.* . in press.

97. Dworzanski, J. P.; Tripathi, A.; Maswadeh, W. M.; Snyder, A. P. *Laboratory MS Identification of Biomarkers from a Fielded Pyrolysis-Gas Chromatography-Ion Mobility Spectrometry (Py-GC-IMS) Proc. of A Major Role for Mass Spectrometry in Homeland Security: Past, Present, and Future in Knoxville, Tennessee* ORNL Ed.; 2003**;** pp30.

98. Loshon, C. A.; Setlow, P., *Can. J. of Microbiol.* **1982**, *39*, 259-62.

99. Meggers, W. F.; Corliss, C. H.; Scribner, B. F. *Tables of Spectral Line Intensities,* second ed.; U.S. Government Printing Office: 1975.

100 Nicholson, W. L.; Setlow, P. *Molecular Biological Methods for Bacillus*, Harwood, C. R.; Cutting, S. M., Eds.; 1st ed.; Wiley: Chichester, 1990.

101. Samek, O.; Beddows, D.; Kaiser, J.; Kukhlevsky, S.; Liska, M.; Telle, H.; Young, J. *Optical Engineer.* **2000,** *39*, 2248-61.

102. Cremers, D. A.; Ebinger, M. H.; Breshears, D. D.; Unkefer, P. J.; Kammerdiener, S. A.; Ferris, M. J.; Catlett, K. M.; Brown, J. R. *J. Environ. Qual.* **2001**, *30*, 2202-06.

103. Beebe, K. R.; Pell, R. J.; Seasholtz, M. B. *Chemometrics A Practical Guide,* John Wiley & Sons, Inc.: New York City, 1998.

BIOGRAPHICAL SKETCH

Emily Mehgan Gibb was born in Blacksburg, VA, on September 18, 1977. She attended Madeira School for girls in McLean, VA, for her first two years of high school. She was involved in student government, Model United Nations, Latin Club and varsity tennis. For her last two years of school she attended Blacksburg High School in Blacksburg, VA. There she was involved in varsity tennis and cross country. She attended the University of Richmond and received her B.S. in chemistry. During her graduate studies in analytical chemistry at the University of Florida she was a delegate and officer in Graduate Student Council.

I certify that I have read this study and that in my opinion it conforms to acceptable standards of scholarly presentation and is fully adequate, in scope and quality, as a dissertation for the degree of Doctor of Philosophy.

James Winefordner, Chair
Graduate Research Professor of Chemistry

I certify that I have read this study and that in my opinion it conforms to acceptable standards of scholarly presentation and is fully adequate, in scope and quality, as a dissertation for the degree of Doctor of Philosophy.

Willard Harrison
Professor of Chemistry

I certify that I have read this study and that in my opinion it conforms to acceptable standards of scholarly presentation and is fully adequate, in scope and quality, as a dissertation for the degree of Doctor of Philosophy.

David Powell
Scientist of Chemistry

I certify that I have read this study and that in my opinion it conforms to acceptable standards of scholarly presentation and is fully adequate, in scope and quality, as a dissertation for the degree of Doctor of Philosophy.

John R. Eyler

John Eyler
Professor of Chemistry

I certify that I have read this study and that in my opinion it conforms to acceptable standards of scholarly presentation and is fully adequate, in scope and quality, as a dissertation for the degree of Doctor of Philosophy.

David Hahn
Associate Professor of Mechanical and
Aerospace Engineering

This dissertation was submitted to the Graduate Faculty of the Department of Chemistry in the College of Liberal Arts and Sciences and to the Graduate School and was accepted as partial fulfillment of the requirements for the degree of Doctor of Philosophy.

May 2004

Dean, Graduate School